Supporting Information

Decorating Zn-MOF-74 on ZIF-8 to Increase Gas Transport and Plasticization Resistance in Mixed-Matrix Membranes

Jin Hui Jo[a], Jieun Lee[a], Eun Ji An[a], Hyomin Choi[a], Hyunmo Jae[b,c], Yubin Lee[d], Miso Kang[d], Jaesung Park[d], Hyuk Taek Kwon[e], Chanmin Lee[f,g], Dongkyu Rho*[c], and Won Seok Chi*[a,h]

[a]Department of Polymer Engineering, Graduate School, Chonnam National Univeristy, 77 Yongbong-ro, Bukgu, Gwangju 61186, Republic of Korea

[b] Department of Chemical and Biochemical Engineering, Yonsei University, 50 Yonsei-ro, Seodaemun-gu, Seoul 03722, republic of Kora

[c] Energy & Environment Division, Korea Institute of Ceramic Engineering and Technology (KICET) 101, Soho-ro, Jinju-si, Gyeongsangnam-do 52851, Republic of Korea

[d] Chemical & Process Technology Division, Korea Research Instituute of Chemical Technology (KRICT), 141, Gajeongro, Yuseong, Daejeion 34114, Republic of Korea

[e] Department of Chemical Engineering, Pukyoung National University, 45 Youngso-ro, Nam-gu, Busan 48513, Republic of Korea

[f] Green Circulation R&D Department, Research Institute of Sustainable Development Technology, Korea Institute of Industrial Technology, 89 Yangdaegiro-gil, Ipjan-myeon, Seobuk-gu, Cheonan-si 31056, Chungcheongnam-do, Republic of Korea

[g] Department of Chemical Engineering, Chung-Ang University, 84 Heokseok-ro, Dongjak-gu, Seoul 31056, Republic of Korea

[h] School of Polymer Science and Engineering, Chonnam National University, 77 Yongbong-ro, Buk-gu, Gwangju 61186, Korea, Email: wschi@jnu.ac.kr

*Corresponding authors

E-mail: rohdk@kicet.re.kr; wschi@jnu.ac.kr

Contents

Gas permeation parameter estimation

Pure gas permeability (P) can be calculated as follows:

$$P = \frac{Vl}{p_2 ART}\left[\left(\frac{dp}{dt}\right)_{ss} - \left(\frac{dp}{dt}\right)_{leak}\right] \quad \textbf{(S1)}$$

where P is the pure gas permeability (Barrer (10^{-10}·cm^3(STP)·cm·cm^{-2}·s^{-1}·cmHg^{-1})), V is the downstream volume (cm^3), l is the average thickness of the membrane (cm), p_2 is the upstream pressure (cmHg), A is the active area of the membrane (cm^2), R is the ideal gas constant, T is the temperature (K), $(dp/dt)_{ss}$ is the steady-state permeation rate (cmHg/s), and $(dp/dt)_{leak}$ is the leak rate (cmHg/s).

The ideal gas selectivity ($\alpha_{A/B}$) for pure gases A and B can be determined by using the following equation:

$$\alpha_{A/B} = \frac{P_A}{P_B}, \quad \textbf{(S2)}$$

where P_A and P_B are the gas permeability values for pure gas species A and B, respectively.

Diffusivity, which is associated with the kinetic diameter and gas transport properties, and solubility, which represents the thermodynamic contribution to gas transport, were also determined to compare the performances of the ZIF-8 and series of ZIF-8@MOF-74 based MMMs. These are respectively defined as follows:

$$D = \frac{l^2}{6\theta} \quad \textbf{(S3)}$$

where D represents the diffusivity (cm^2/s), l represents the thickness of the membrane (cm), and θ represents the time lag (s).

$$P = D \times S \tag{S4}$$

where P is the pure gas permeability (Barrer), D is the diffusivity (cm^2/s), and S is the solubility ($cm^3(STP)/cm^3 \cdot atm$).

The respective diffusivity-selectivity $(\alpha_{A/B}(D))$ and solubility-selectivity $(\alpha_{A/B}(S))$ values for gas species A and B can also be estimated as follows:

$$\alpha_{A/B}(D) = \frac{D_A}{D_B} \tag{S5}$$

$$\alpha_{A/B}(S) = \frac{S_A}{S_B} \tag{S6}$$

where D_A and D_B are the diffusivity (cm^2/s), and S_A and S_B are the solubility ($cm^3(STP)/cm^3 \cdot atm$) for gas species A and B, respectively.

Mixed-gas separation performance test

Membrane films were masked with epoxy (Devcon 20845, Danvers, MA, USA) on a copper plate (5.0 cm in diameter). The effective permeation area was approximately 2.0 cm^2, which was determined by digital image analysis using ImageJ software. The thickness of the membrane films was approximately 60-70 μm, as measured with a digital micrometer (547-401, Mitutoyo, Japan). Mixed-gas permeation measurements were performed using a modified constant pressure, variable volume method. An equimolar CO_2/CH_4 mixture was tested at 4 atm and 25 ^oC, with upstream flow rates regulated by mass flow controllers (5850E Series, Brooks Instrument, PA, USA). Helium was used as a carrier gas to sweep the permeate gas to a gas chromatograph (DS6200, Donam Instruments, Korea) equipped with a thermal conductivity detector. The downstream flow rate was measured using a flow gauge. To minimize concentration polarization at the membrane film surface, the stage cut was maintained below 1 % during all mixed-gas measurements. In addition, for comparison purposes, the pure-gas permeabilities of CO_2 and CH_4 were measured at 2 atm and 25 ^oC using the same apparatus.

Error propagation

The uncertainty of permeability coefficients (σ_P) is determined as follows:

$$\sigma_P = P\sqrt{\left(\frac{\sigma_{V_D}}{V_D}\right)^2 + \left(\frac{\sigma_l}{l}\right)^2 + \left(\frac{\sigma_{p_2}}{p_2}\right)^2 + \left(\frac{\sigma_T}{T}\right)^2 + \left(\frac{\sigma_A}{A}\right)^2 + \Delta^2} \quad \textbf{(S7)}$$

In **Eq. S7**, the relative uncertainty of the downstream volume ($\frac{\sigma_{V_D}}{V_D}$) is assumed to be 3%; the uncertainty of the membrane thickness (σ_l) is determined by calculating the standard deviation of seven measurements of the membrane thickness (l), the uncertainty of the upstream pressure (σ_{p_2}), as reported by the downstream transducer and specified by the manufacturer, is fixed at 0.05 psi, p_2 is fixed at 15 psi; the uncertainty in the active area (σ_A) was estimated using the standard deviation from 10 measurements and the uncertainty in temperature (σ_T) was considered negligible due to excellent control maintaining the deviation within 0.01 K from the target temperature and the relative uncertainty ($\left[\left(\frac{dp}{dt}\right)_{ss} - \left(\frac{dp}{dt}\right)_{leak}\right]$ denoted as Δ) is assumed to be 1%.

Synthesis of Zn-metal organic framework (MOF)-74 nanoparticles

These were synthesized according to the method reported in reference [1] Briefly, zinc nitrate hexahydrate (0.452 g) and 2,5-dihydroxyterephthalic acid (DHTA) (0.1 g) were dissolved in 12 mL of dimethyl formamide (DMF)/ethanol (EtOH)/deionized (DI) water (10/1/12, v/v/v). The solution was sealed in a 50 mL Teflon-lined autoclave and heated at 110 ^{o}C for 20 h. The product was collected by centrifugation and washed with DMF and methanol (MeOH) three times each. The obtained Zn-MOF-74 nanoparticles were dried in an oven at 60 ^{o}C overnight, twice, to remove any residual solvents.

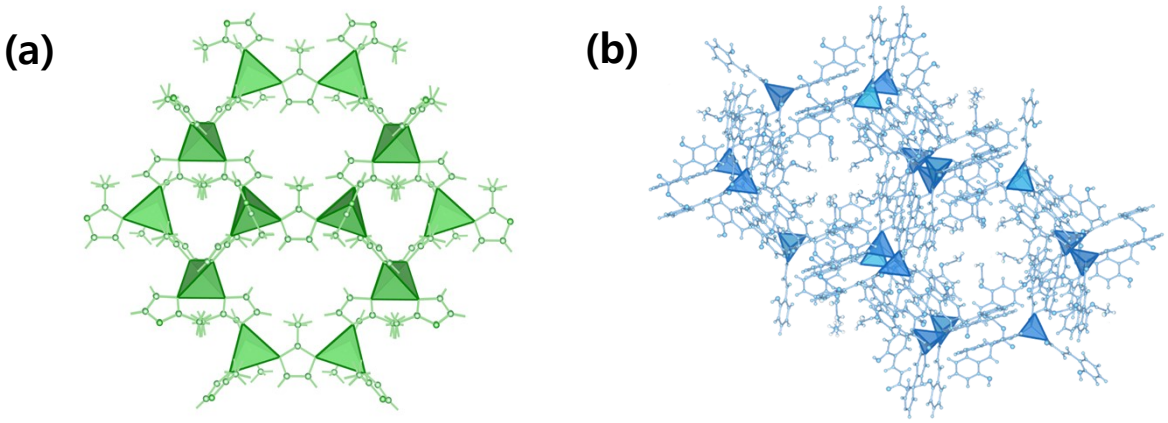

Fig. S1. The crystal structures of (a) zeolitic imidazolate framework-8 (ZIF-8) and (b) Zn-MOF-74. The crystallographic data were obtained from references [2] and[3] using CIF files sourced from the Crystallography Open Database.

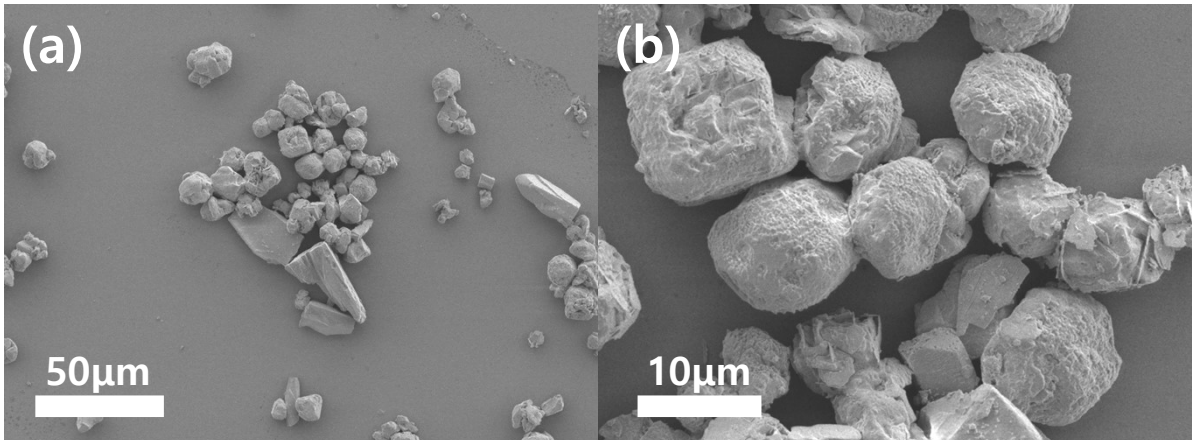

Fig. S2. FE-SEM images of micron-sized Zn-MOF-74 particles at (a) low resolution and (b) high resolution.

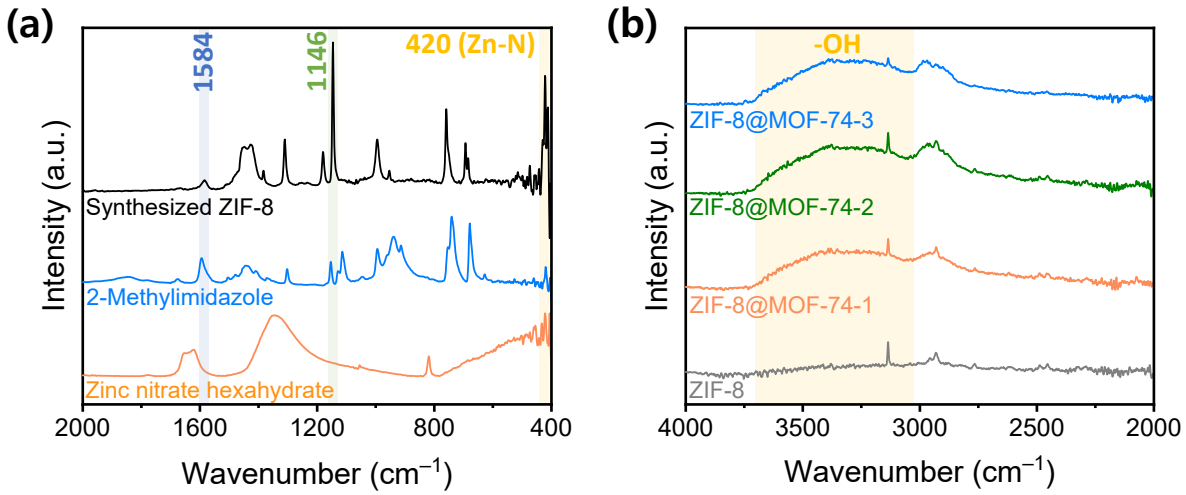

Fig. S3. (a) FT-IR spectra for 2-methylimidazole, zinc nitrate hexahydrate, and ZIF-8 nanoparticles and (b) ZIF-8 and ZIF-8@MOF-74 nanoparticles in the wavenumber ranges from 4000-380 cm^{-1} and 4000-2000 cm^{-1}, respectively.

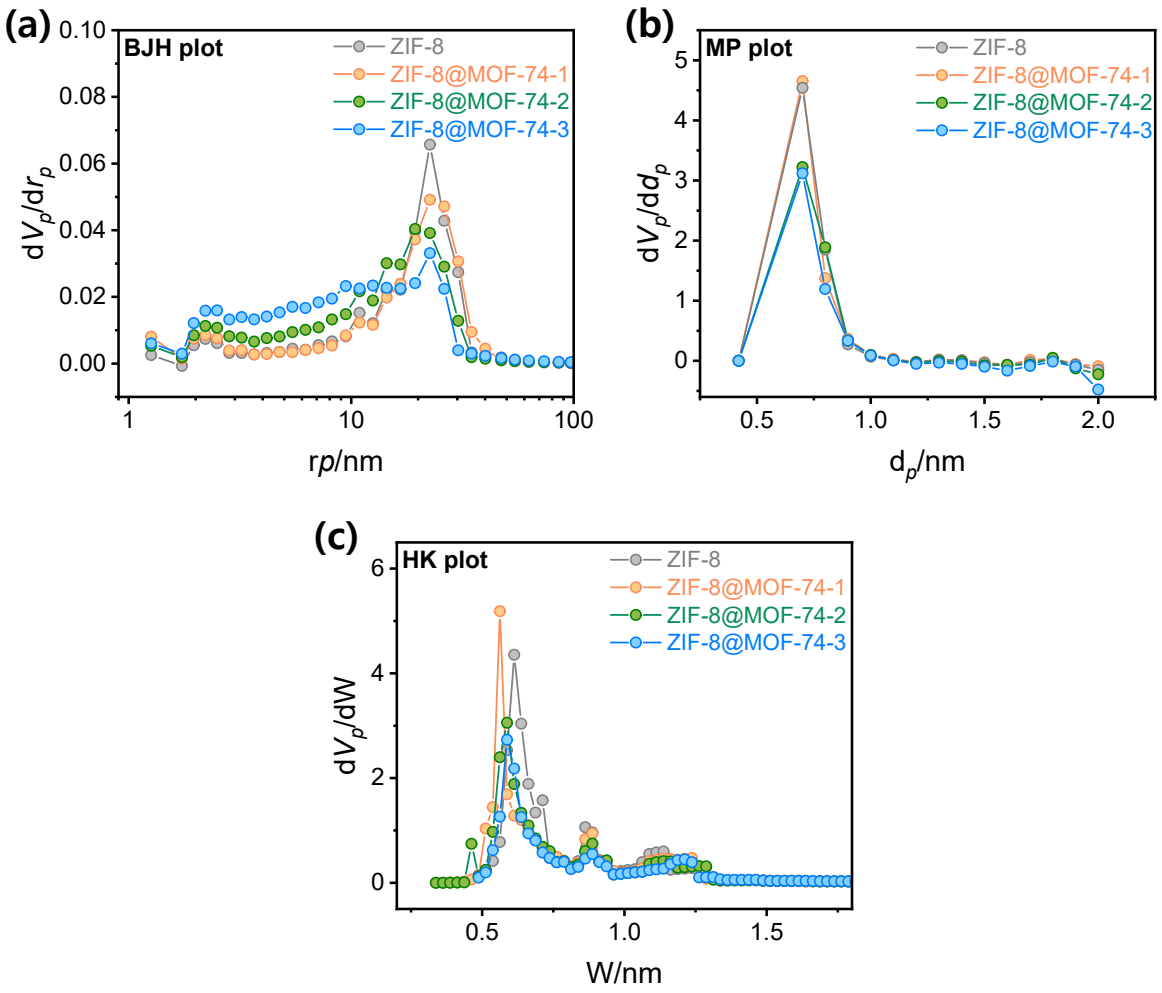

Fig. S4. Pore size distributions for ZIF-8 and series of ZIF-8@MOF-74 nanoparticles (a) Barrett-Joyner-Halenda (BJH) plots, (b) Micropore (MP) plots, and (c) Horvath-Kawazoe (HK) plots.

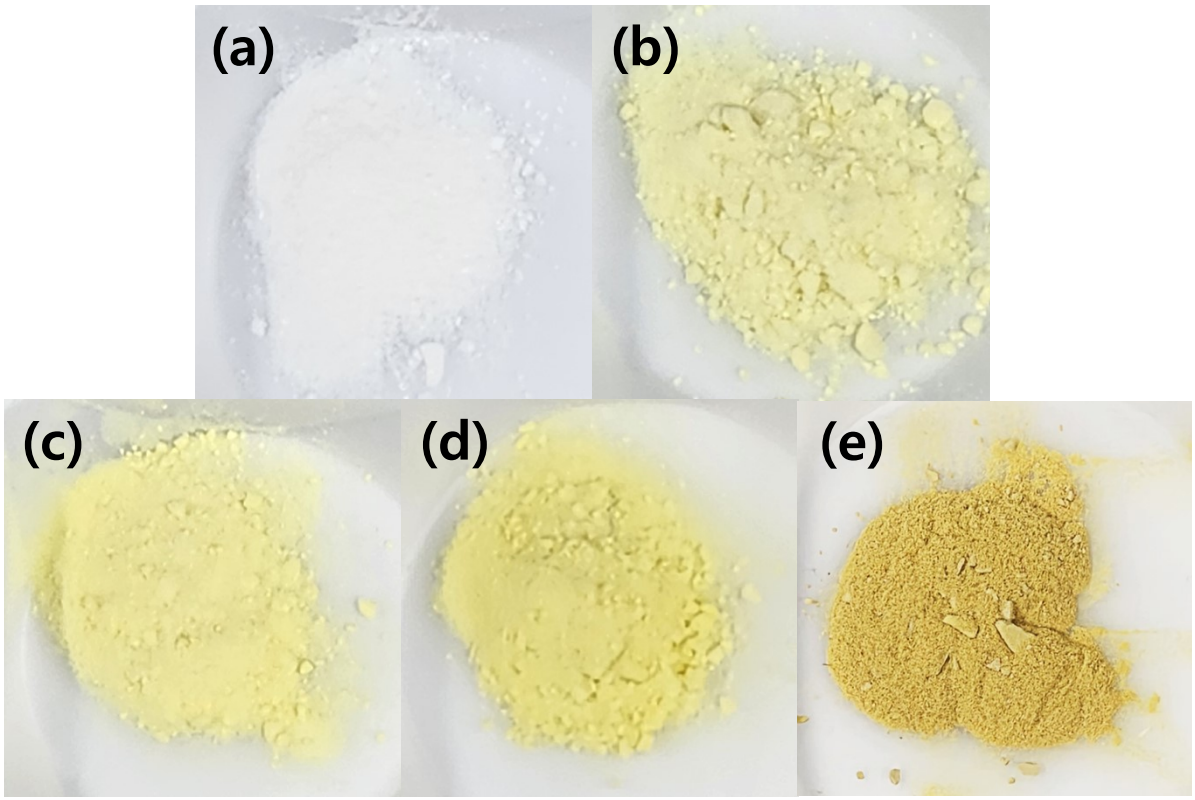

Fig. S5. Optical images of (a) ZIF-8, (b) ZIF-8@MOF-74-1, (c) ZIF-8@MOF-74-2, (d) ZIF-8@MOF-74-3 and (e) Zn-MOF-74 samples. ZIF-8@MOF-74-1, ZIF-8@MOF-74-2, and ZIF-8@MOF-74-3 were synthesized with ZIF-8/DHTA concentration ratios of 18:1, 12:1, and 6:1, respectively.

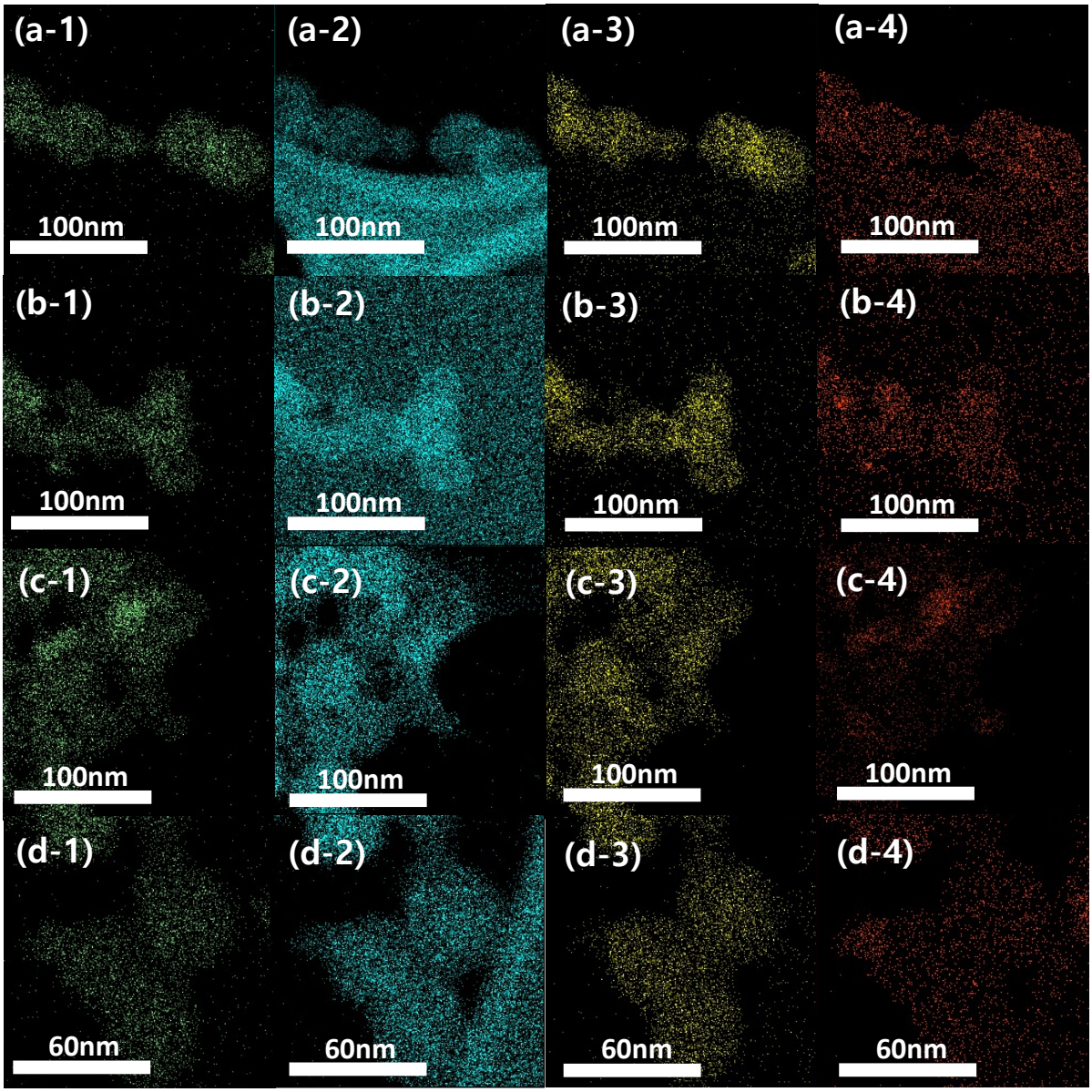

Fig. S6. EDS mapping images of (a) ZIF-8, (b) ZIF-8@MOF-74-1, (c) ZIF-8@MOF-74-2, and (d) ZIF-8@MOF-74-3: 1 = Zn, 2 = C, 3 = N, and 4 = O.

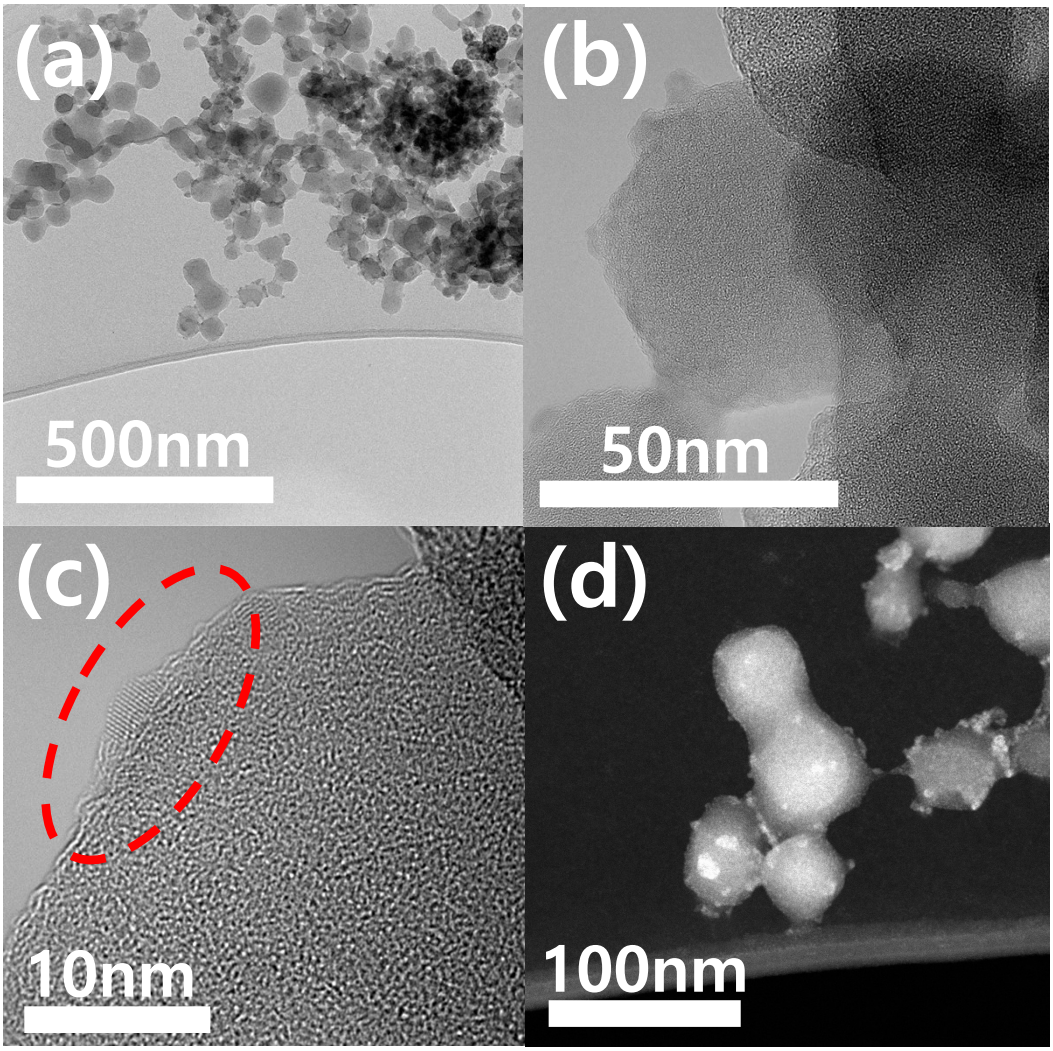

Fig. S7. HAADF-TEM images of ZIF-8@MOF-74-3 nanoparticles with (a) low resolution and (b, c) high resolution images and (d) Scanning TEM (STEM) image.

The low-magnification HAADF-TEM image (**Fig. S7a**) reveals small nanoparticles decorating the surface of a larger core particle. The high-magnification HAADF-TEM and STEM images (**Fig. S7b-d**) clearly illustrate the distinct lattice boundary at the ZIF-8 and MOF-74 interface, providing direct evidence of Zn-MOF-74 growth on the ZIF-8 surface [4,5].

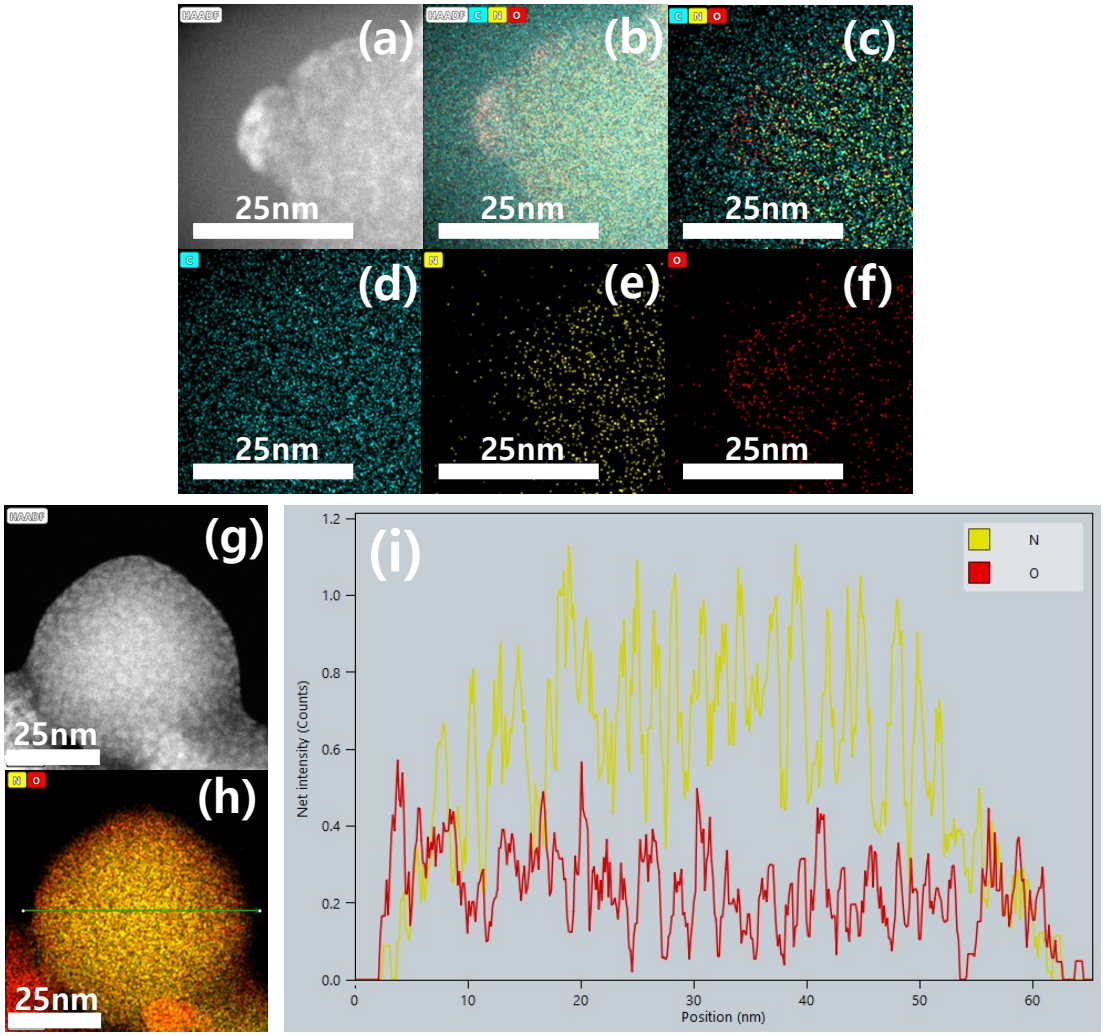

Fig. S8. (a, g) HAADF-STEM images of ZIF-8@MOF-74-3 nanoparticles. (b, c) HAADF-STEM images overlaid with EDS elemental mapping images of C (cyan), N (green), and O (red). (d-f) Individual EDS elemental mapping images of (d) C, (e) N, and (f) O, (h) STEM-EDS elemental overlay image showing the line-scan path for N (yellow) and O (red). (i) EDS line-scan profiles of ZIF-8@MOF-74-3 nanoparticles.

HAADF-EDS elemental mapping of the same nanoparticle (**Fig. S8a-f**) shows a strong oxygen signal confined to the decorating Zn-MOF-74, while zinc and carbon are distributed throughout. Quantitative line-scan profiles across the nanoparticle (**Fig. S8g-i**) further confirm the morphology. Nitrogen (in 2MeIM) is concentrated in the core, whereas oxygen (in DHTA) is enriched at the surface.

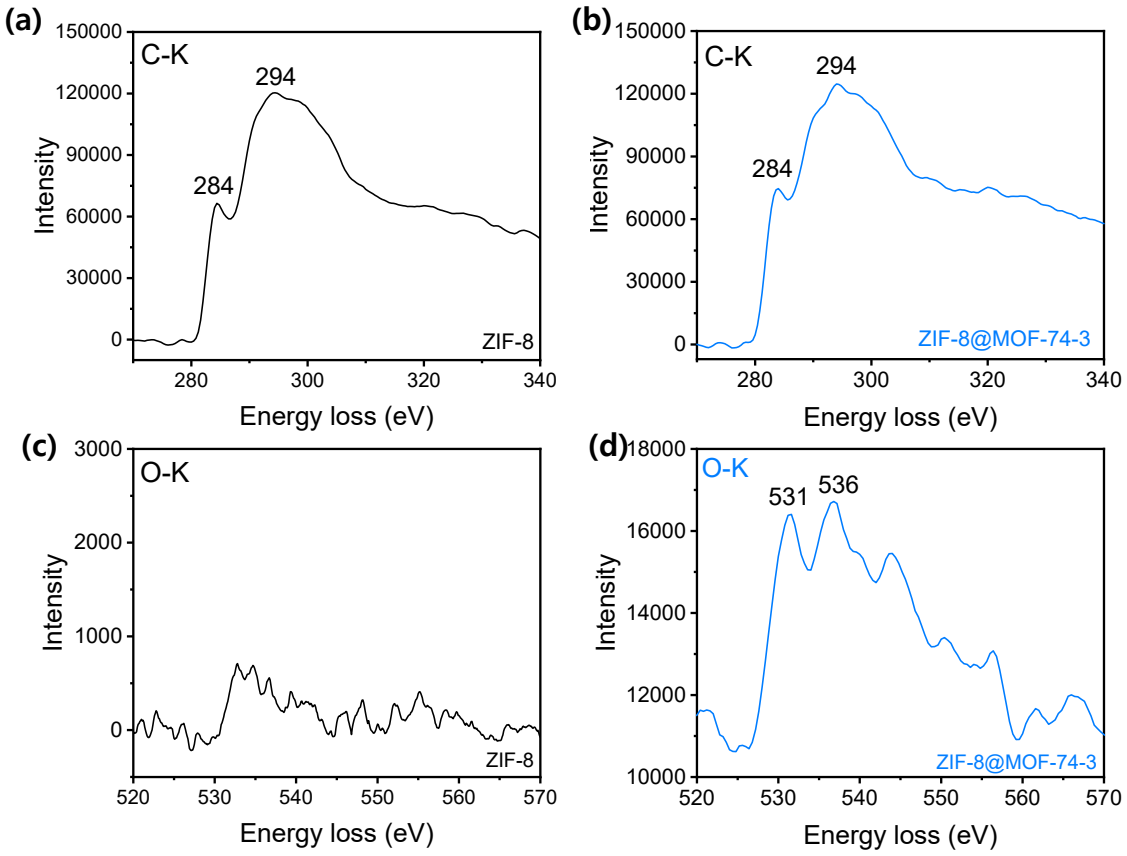

Fig. S9. Electron energy loss spectroscopy (EELS) spectra of (a,c) pristine ZIF-8 and (b,d) ZIF-8@MOF-74-3 for (a, b) C-K and (c, d) O-K edge evolution.

For deeper structure insight, electron energy-loss spectroscopy (EELS) was conducted on pristine ZIF-8 and ZIF-8@MOF-74-3 (**Fig. S9**). The C-K edges (**Fig. S9a,b**) exhibit similar π* features at ~284 eV (C=N and C=C bonds) for both samples, confirming the existence of the ZIF-8 despite the formation of the Zn-MO-74. Notably, the O-K edge of ZIF-8 (**Fig. S9c**) shows negligible intensity (520-550 eV), attributable to trace adsorbed H_2O or contamination, consistent with its oxygen-free composition. In contrast, ZIF-8@MOF-74-3 (**Fig. S9d**) show more than ~8-fold intensity increase, with a prominent pre-edge peak at ~531 eV assigned to 1s to σ* transitions in Zn-O and -COO^- moieties show definitive evidence of Zn-MOF-74 formation on the ZIF-8 surface [6].

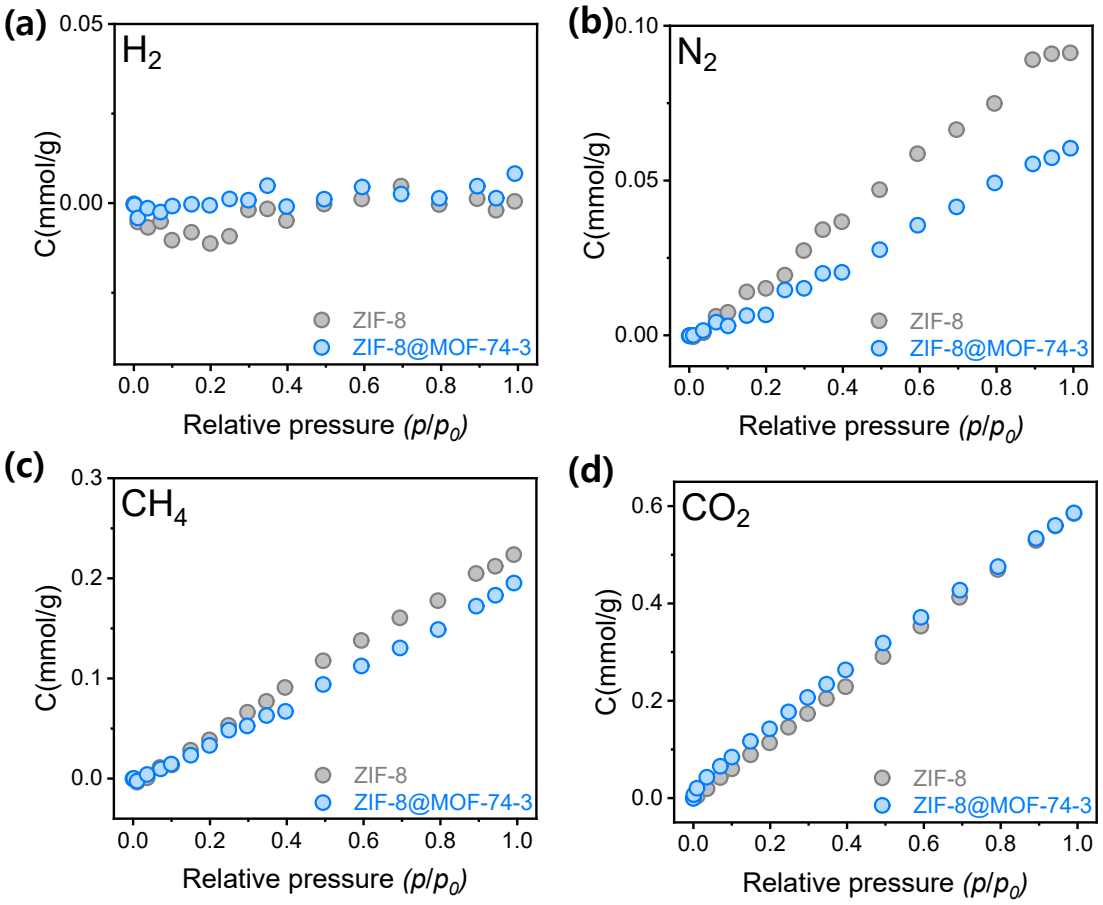

Fig. S10. (a) H_2, (b) N_2, (c) CH_4, and (d) CO_2 gas sorption isotherms at 308.15K for ZIF-8 (Grey) and ZIF-8@MOF-74-3 (Blue) nanoparticles.

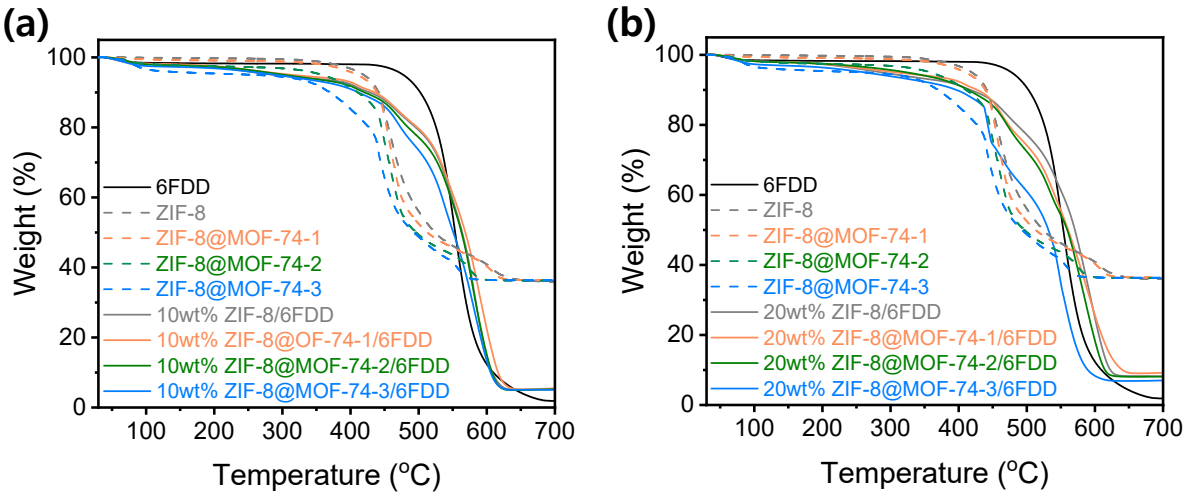

Fig. S11. TGA curves for (a) ZIF-8 and ZIF-8@1-3 nanoparticles, pure 6FDD, and the 10 wt% ZIF-8/6FDD and series of 10 wt% ZIF-8@MOF-74/6FDD MMMs and (b) ZIF-8 and ZIF-8@MOF-74 nanoparticles, pure 6FDD, and the 20 wt% ZIF-8/6FDD and series of 10 wt% ZIF-8@MOF-74/6FDD MMMs measured under an air atmosphere.

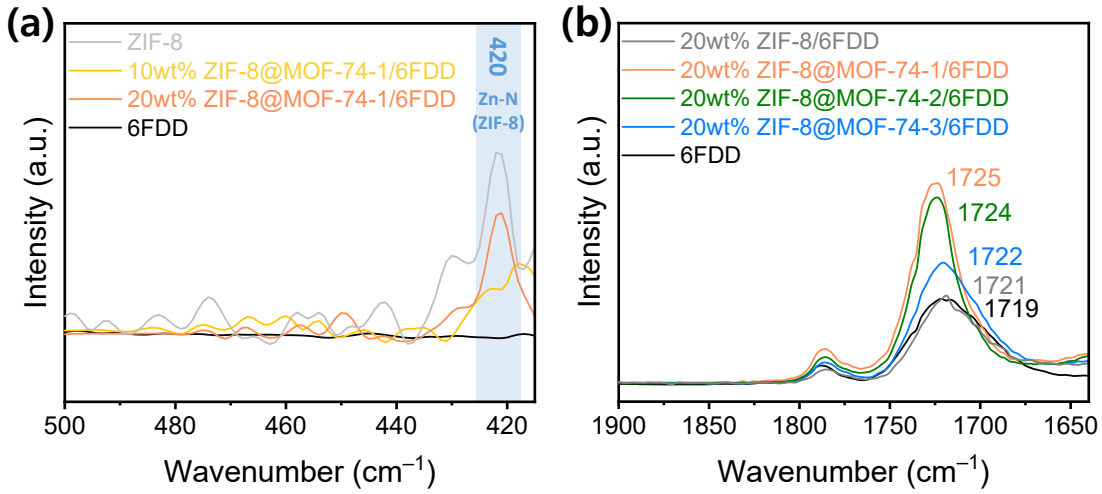

Fig. S12. FT-IR spectra for (a) ZIF-8 nanoparticle, 6FDD and the 10 and 20 wt% ZIF-8@MOF-74-1/6FDD MMMs and (b) 6FDD membrane, 20wt% ZIF-8/6FDD and series of 20 wt% ZIF-8@MOF-74-3/6FDD MMMs in the wavenumber ranges from 500-415 cm^{-1} and 1900-1640 cm^{-1}, respectively.

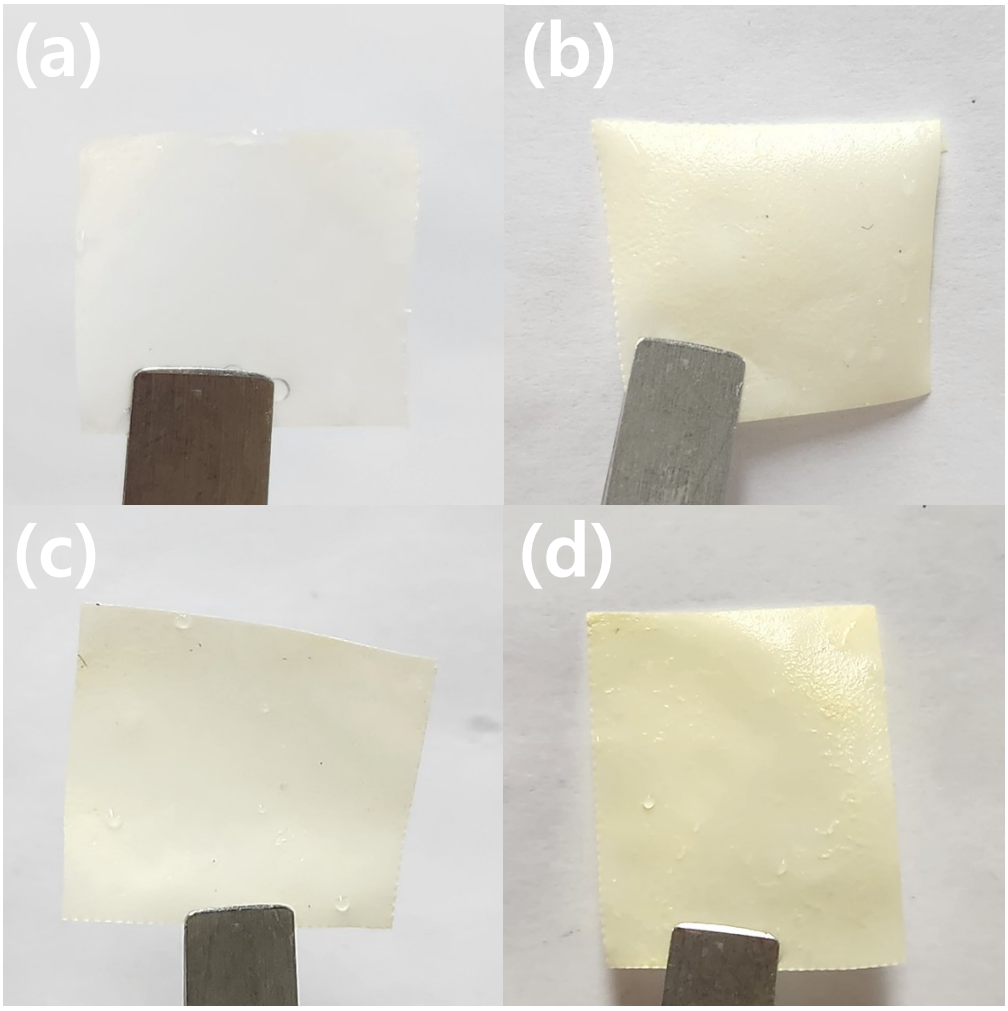

Fig. S13. Optical images of the (a) 20 wt% ZIF-8/6FDD, (b) 20 wt% ZIF-8@MOF-74-1/6FDD, (c) 20 wt% ZIF-8@MOF-74-2/6FDD, and (d) 20 wt% ZIF-8@MOF-74-3/6FDD MMMs.

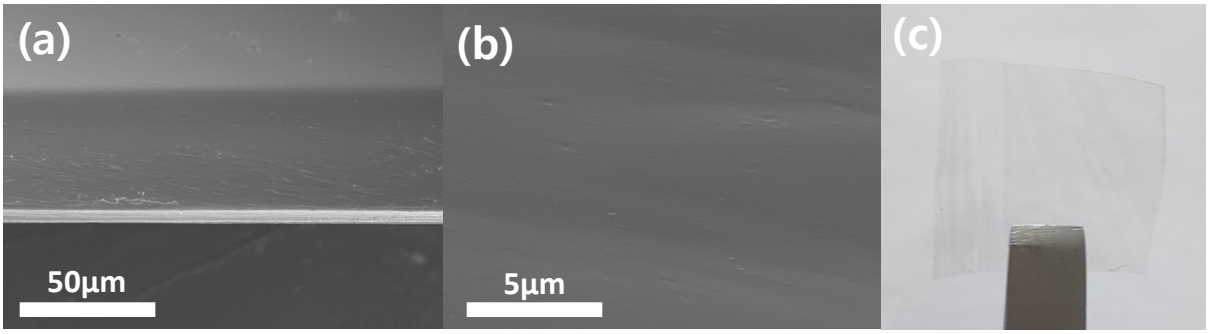

Fig. S14. Cross-sectional SEM images at (a) low and (b) high resolution and (c) an optical image of the 6FDD polyimide membrane.

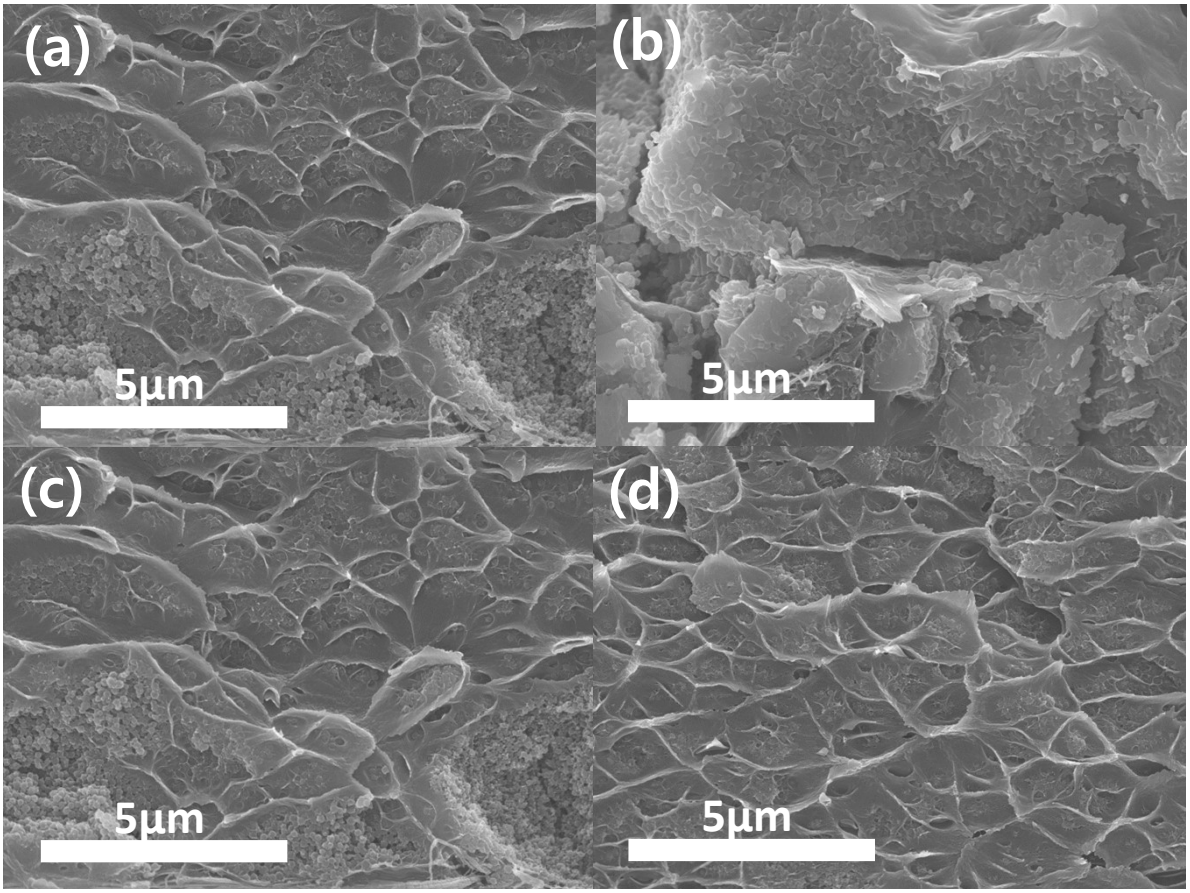

Fig. S15. Cross-sectional SEM images of the bottom surfaces of the (a) 20 wt% ZIF-8/6FDD, (b) 20 wt% ZIF-8@MOF-74-1/6FDD, (c) 20 wt% ZIF-8@MOF-74-2/6FDD, and (d) 20 wt% ZIF-8@MOF-74-3/6FDD MMMs.

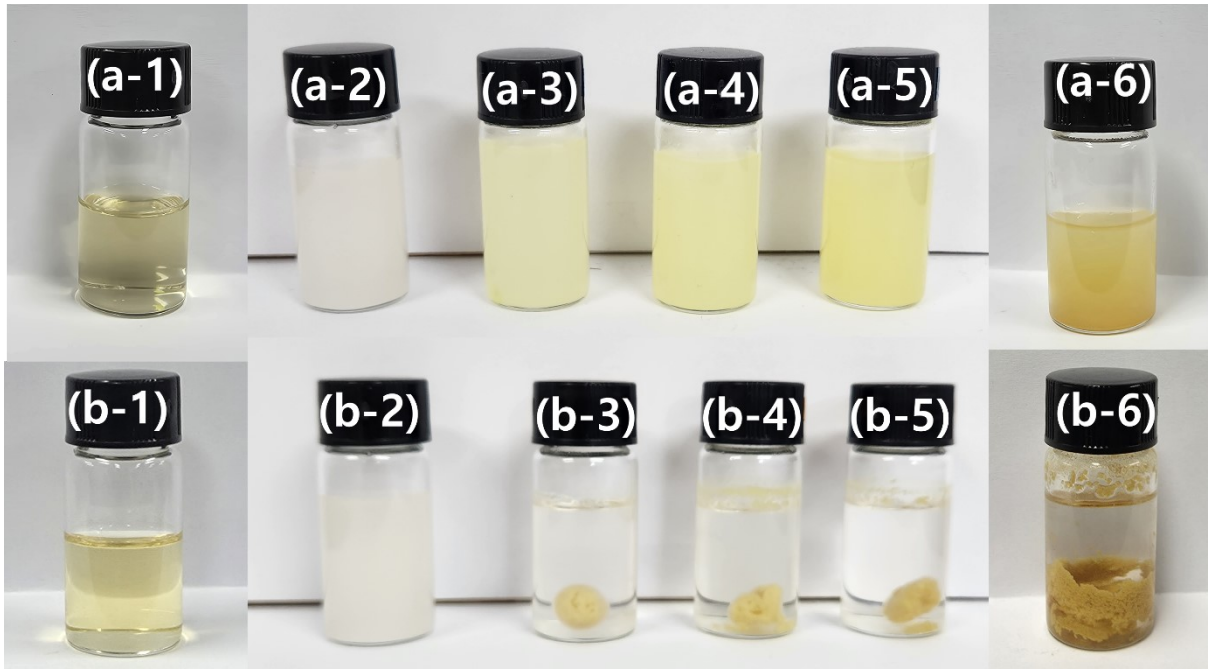

Fig. S16. Compatibility test of the ZIF-8 and ZIF-8@MOF-74 powders in 6FDD polymer solution (a) immediately after addition and (b) after stirring overnight. 1 = DHTA ligand, 2 = ZIF-8, 3 = ZIF-8@MOF-74-1, 4 = ZIF-8@MOF-74-2, 5 = ZIF-8@MOF-74-3 and 6 = Zn-MOF-74.

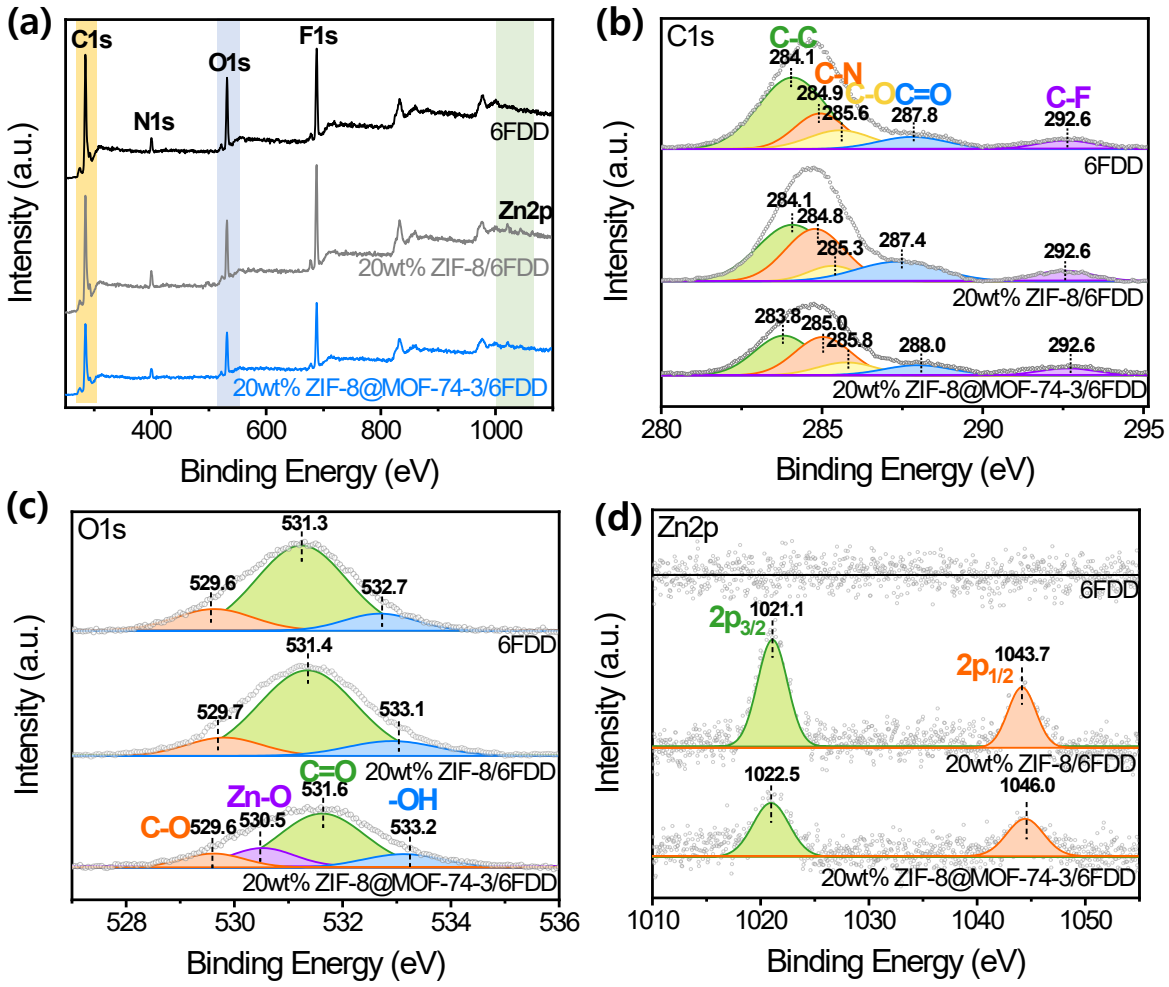

Fig S17. a) Survey XPS spectra and high-resolution XPS spectra for the b) C 1s, c) O 1s, and d) Zn 2p of pristine 6FDD, 20 wt% ZIF-8/6FDD, and 20 wt% ZIF-8@MOF-74-3/6FDD MMMs with deconvolution of the major peak.

XPS analysis was performed for pristine 6FDD, 20 wt% ZIF-8/6FDD, and 20 wt% ZIF-8@MOF-74-3/6FDD MMM to investigate the interfacial interactions between the carboxylic acid groups of 6FDD and the Zn-MOF-74 moieties, particularly the open metal sites (OMS) and hydroxyl functionalities. The survey spectra and high-resolution C 1s, O 1s, and Zn 2p spectra are shown in **Fig. S17**. As shown in the C 1s spectrum of pristine 6FDD was deconvoluted into five components corresponding to C-C, [7,8] C-N, [8,9] C-O, [7–9] C=O [7–9] and C-F [7] bonds at 284.1, 284.9, 285.6, 287.8, and 292.6 eV for pristine 6FDD membrane

(**Fig. S17b**). The O 1s spectra was deconvoluted to C-O, [9,10] C=O [9,10] and -OH [10] for the pristine 6FDD membrane with 529.6, 531.3, and 532.7 eV. For the 20 wt% ZIF-8@MOF-74-3/6FDD MMM, an additional O 1s component appeared at 530.5 eV, which can be assigned to the Zn-O bond associated with the DHTA ligand of Zn-MOF-74 (**Fig. S17c**). [11] In the Zn 2p spectra, no Zn signal was observed for pristine 6FDD, whereas both MMMs exhibited characteristic 2p 3/2 and 2p 1/2 (**Fig. S17d**). [11,12] Notably, the binding energy of C 1s and O 1s moved higher for the 20 wt% ZIF-8@MOF-74-3/6FDD MMM compared to pristine 6FDD and 20 wt% ZIF-8/6FDD MMM. These shifts indicate changes in the local electronic environment, suggesting interactions between the polymer functional groups and the MOF surface. [13–15] In particular, an increase in binding energy in the Zn 2p peaks implies that Zn electron density decreased due to the coordination with the carboxylic acid polymer matrix. [16]

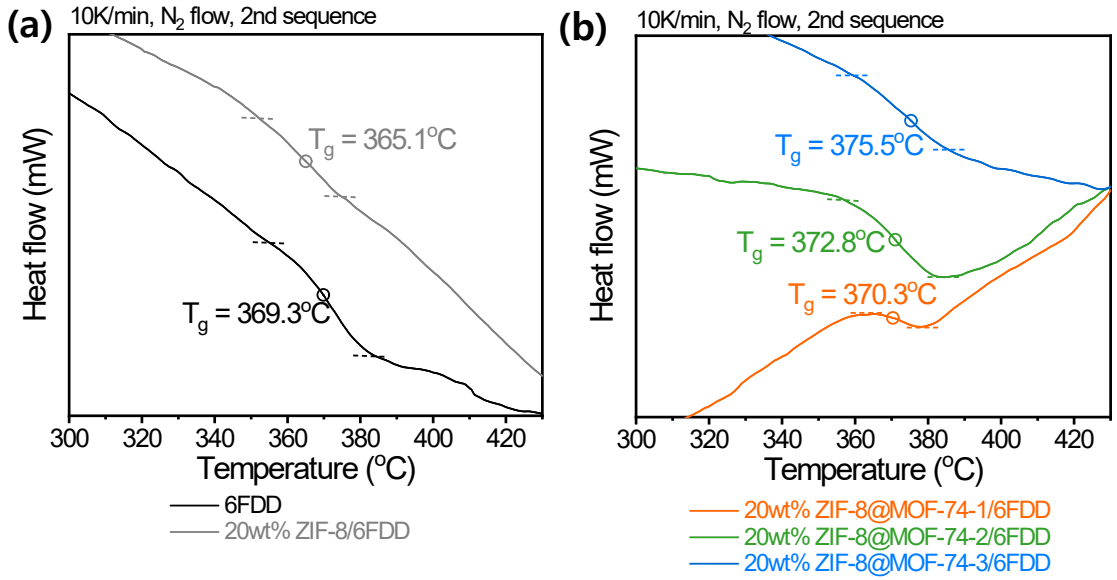

Fig. S18. DSC curves of (a) pristine 6FDD and 20wt% ZIF-8/6FDD MMM and (b) series of 20 wt% ZIF-8@MOF-74 MMMs under nitrogen atmosphere with 2nd sequence.

DSC analysis (**Fig. S18**) shows the T_g of the 20 wt% ZIF-8@MOF-74/6FDD MMMs increases compared to pristine 6FDD and the 20 wt% ZIF-8/6FDD MMM. Notably, the 20 wt% ZIF-8/6FDD MMM exhibits a slightly decreased T_g relative to pristine 6FDD, which can be attributed to poor interfacial compatibility between ZIF-8 and the polymer matrix. This weak interaction likely induces localized polymer chain relaxation near the filler surface, leading to enhanced segmental mobility [17].

In contrast, the elevated T_g observed for the series of 20 wt% ZIF-8@MOF-74/6FDD MMMs indicates restricted polymer chain mobility, suggesting stronger interfacial interactions between the MOF surface and the polymer matrix. Furthermore, the progressive increase in T_g with increasing Zn-MOF-74 content within the ZIF-8@MOF-74 structure supports enhanced interfacial confinement effects.

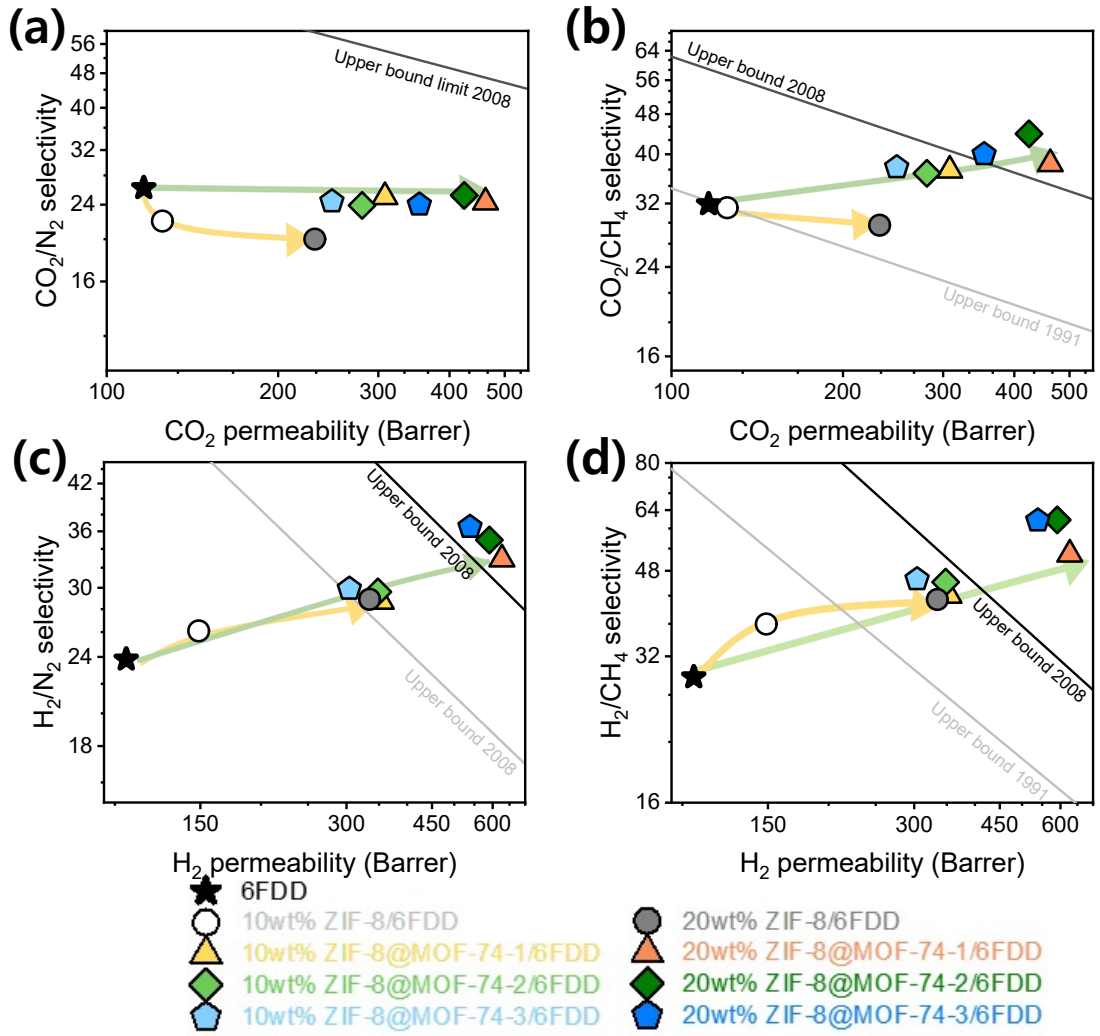

Fig. S19. a) CO_2/N_2, b) CO_2/CH_4, c) H_2/N_2, and d) H_2/CH_4 gas separation performances of pure 6FDD polyimide membrane, ZIF-8/6FDD MMM, and series of ZIF-8@MOF-74/6FDD MMMs with 10 or 20 wt% MOF loading at 15 psi and 35 °C with the upper-bound limits

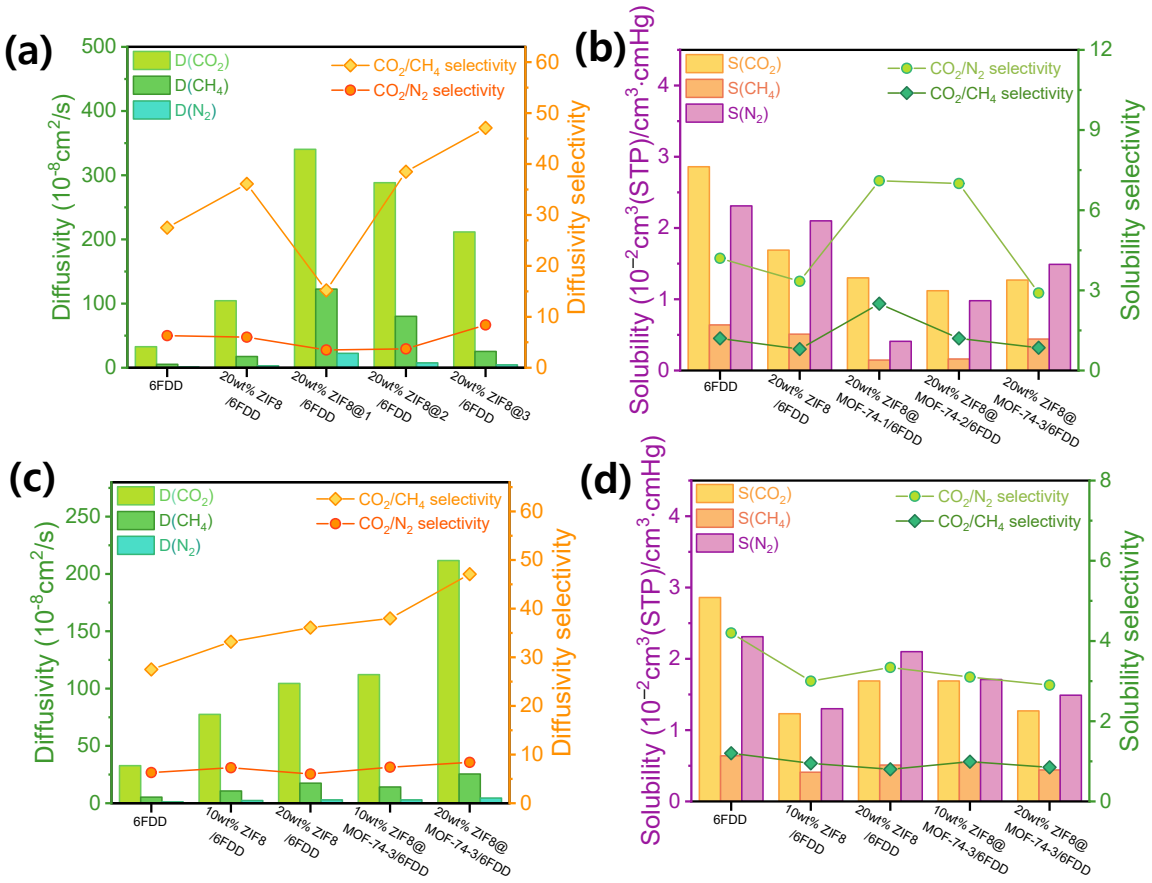

Fig. S20. (a, c) N_2, CH_4, CO_2 diffusivities and CO_2/N_2 and CO_2/CH_4 diffusivity-selectivity values and (b, d) N_2, CH_4, and CO_2 solubilities, and CO_2/N_2 and CO_2/CH_4 solubility-selectivity values, for the (a, b) 6FDD polyimide membrane, 20 wt% ZIF-8/6FDD and series of 20 wt% ZIF-8@MOF-74/6FDD MMMs and (c, d) 6FDD polyimide membrane,10 and 20 wt% ZIF-8/6FDD and ZIF-8@MOF-74-3/6FDD MMMs. Measurements were conducted at 15 psi and 35 °C

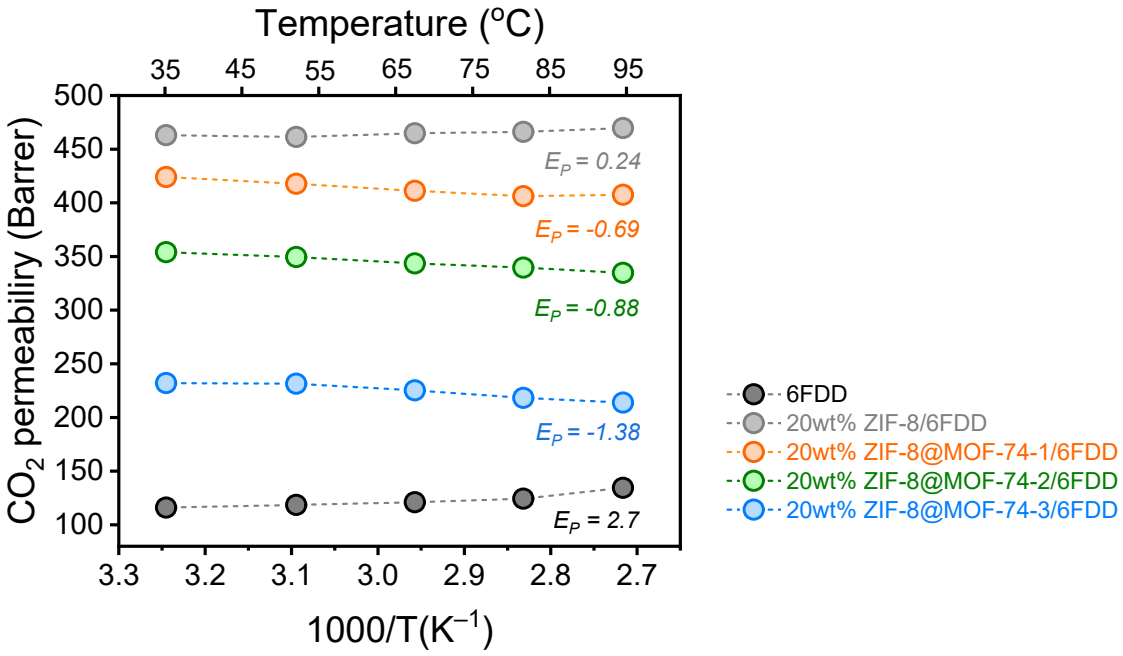

Fig. S21. Arrhenius plots of CO_2 permeability for pristine 6FDD, 20 wt% ZIF-8/6FDD, and series of 20 wt% ZIF-8@MOF-74/6FDD MMMs measured at 15 psi with different temperatures (35-95 °C). The apparent activation energies for CO_2 permeability (E_p) were determined from the slopes of the linear fits according to the Arrhenius equation.

The apparent activation energies for CO_2 permeability (E_p) were determined from the temperature dependence of permeability using the Arrhenius equation **(S8)** for pristine 6FDD, 20 wt% ZIF-8/6FDD, and series of 20 wt% ZIF-8@MOF-74/6FDD MMMs.

$$lnk = -(E_p/R)(1/T)\, lnA \quad \textbf{(S8)}$$

where, k is the rate constant, A is the pre-exponential factor, R is the gas constant with 8.134 J/K·mol, T is the temperature in K (Kelvin), and E_p is the activation energy for the CO_2 permeability.

The temperature dependence of CO_2 permeability (35-95 °C) provides important insight into the governing transport mechanisms (**Fig. S21**). Pristine 6FDD exhibits a positive apparent

activation energy (E_p = +2.7 kJ /mol). Incorporation of ZIF-8 reduces the activation energy to E_p = +0.24 kJ /mol, indicating a lowered effective diffusion barrier. This decrease is attributed to the introduction of intrinsic microporous transport pathways within ZIF-8 and locally increased free volume at relatively weak polymer-filler interfaces. Moreover, as temperature increases, polymer chains undergo enhanced segmental relaxation, increasing free-volume fluctuations and facilitating gas diffusion. [18]

Surprisingly, ZIF-8@MOF-74-3/6FDD MMM exhibit a further decrease in activation energy (E_p = −1.38 k/mol). In conventional glassy membranes, increasing temperature promotes polymer chain relaxation and typically increases permeability. This phenomenon is due to the increase of sorption sites (OMSs) and strong interfacial adhesion between the Zn-MOF-74 and the polyimide matrix (supported by **Fig. S15-18**), evidence of coordination and hydrogen bonding, which restricts temperature-induced chain relaxation. [19–21] Such interfacial confinement restricts temperature-induced polymer chain relaxation and reduces the temperature sensitivity of diffusion. This phenomenon is noteworthy, as negative apparent activation energies for CO_2 permeability are relatively uncommon in membrane systems. [21,22]

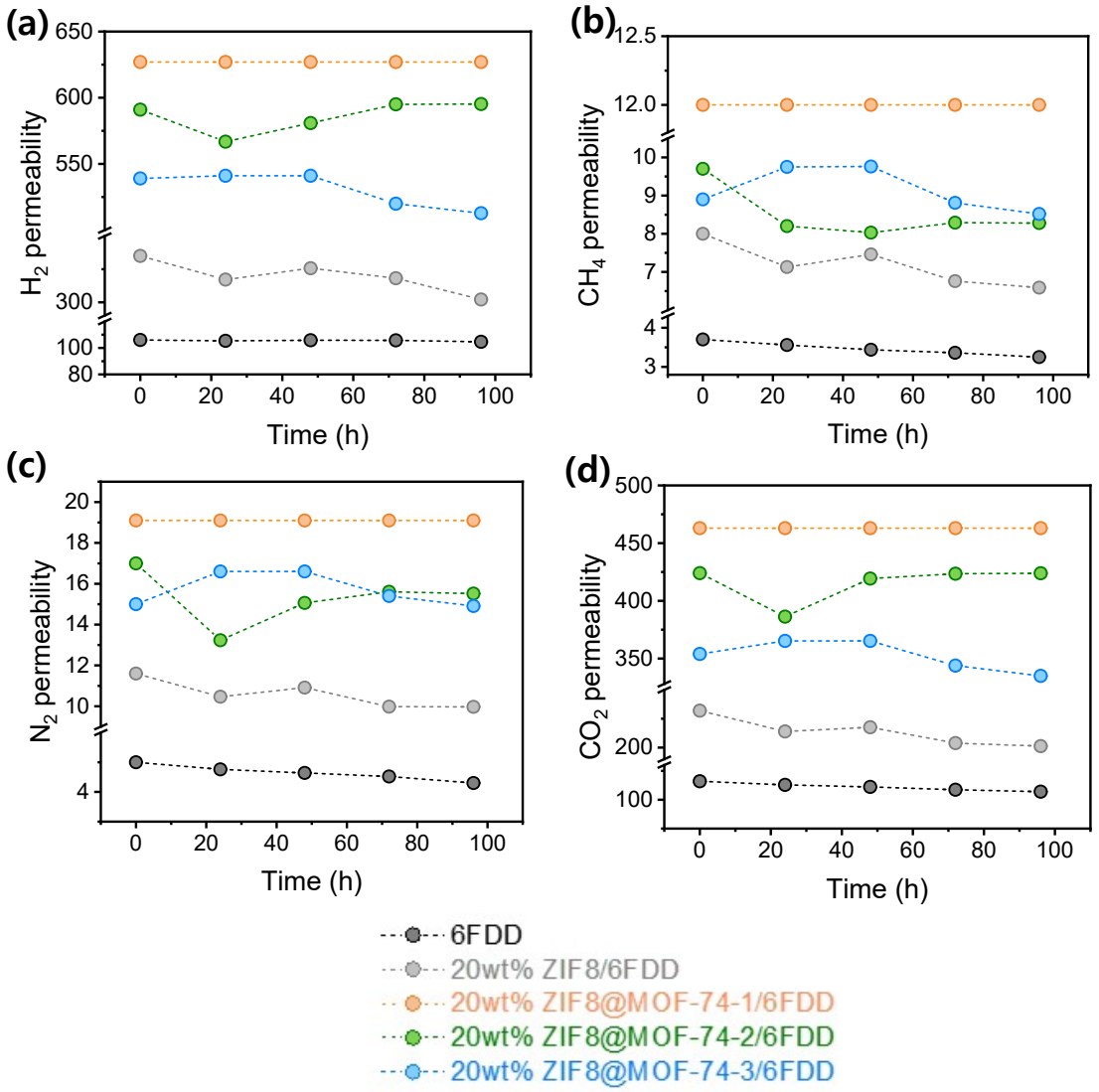

Fig. S22. Long-term gas permeability of pristine 6FDD, 20 wt% ZIF-8/6FDD, and series of 20 wt% ZIF-8@MOF-74/6FDD MMMs for 96 hours at 15 psi and 35 °C.

Maxwell model Calculations

The Maxwell model was used to estimate the theoretical gas permeability limits of the MMMs based on the properties of the polymer matrix and the dispersed filler phase as follows:

$$P_{eff} = P_c\left[\frac{P_d + 2P_c - 2\Phi_d(P_c - P_d)}{P_d + 2P_c + \Phi_d(P_c - P_d)}\right], \quad \textbf{(S9)}$$

where P_{eff} is the effective permeability of the MMM, and P_c and P_d are the permeabilities of the continuous (polymer) and dispersed (MOF) phases, respectively.

The volume fraction (Φ_d) of the MOFs was calculated as follows:

$$\Phi_d = \frac{w_d/\rho_d}{w_d/\rho_d + w_c/\rho_c}, \quad \textbf{(S10)}$$

where w_d and w_c are the weights and ρ_d and ρ_c are the densities of the dispersed and continuous phases, respectively. The reported ρ_d values for 6FDD and ZIF-8 are 1.30 and 0.95 g/cm^3, respectively [23].

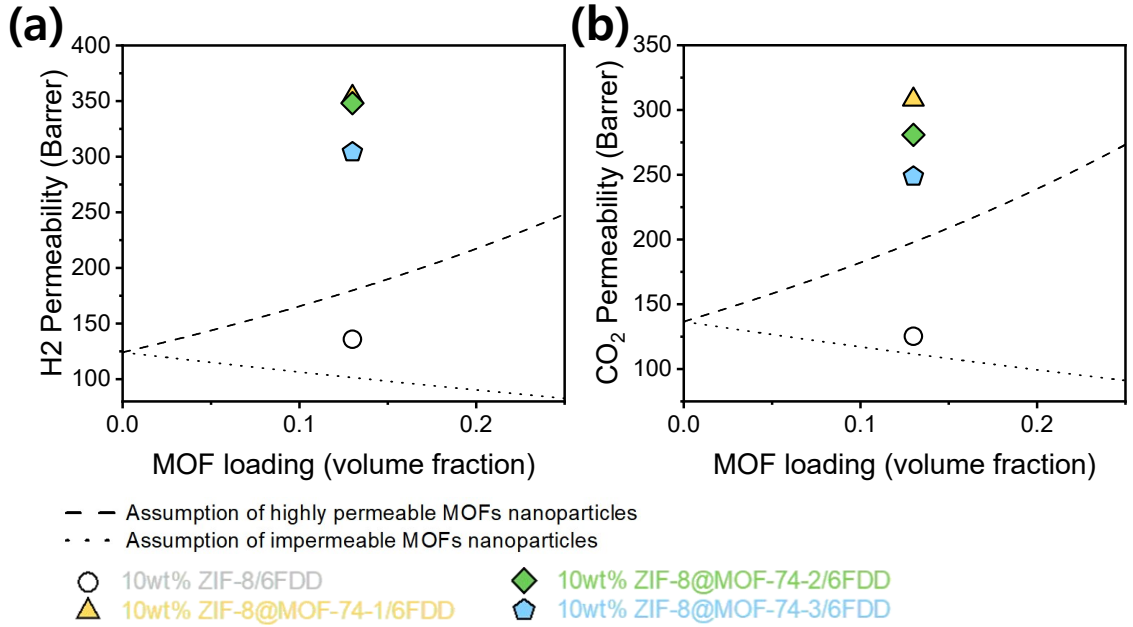

Fig. S23. H_2 and CO_2 permeabilities as a function of MOF volumetric loading for the 10 wt% 6FDD/ZIF-8 and series of 6FDD/ZIF-8@MOF-74 MMMs at 15 psi and 35 °C. The permeabilities of the MMMs are compared with the theoretical values estimated using the Maxwell model in terms of the respective upper (P_d=∞) and lower (P_d= 0) permeability limits.

The Maxwell model is based on several simplifying assumptions: (i) filler particles are approximately spherical and uniformly dispersed at low volume fractions; (ii) the polymer and filler phases are homogeneous and non-porous, each characterized by a single, spatially uniform transport coefficient; and (iii) polymer–filler interfaces are ideal, such that they do not introduce additional transport resistances or pathways and the filler particles remain effectively isolated and non-interacting. Under these conditions, the model provides a reliable prediction of the effective permeability of mixed-matrix membranes (MMMs). Deviations observed at higher filler loadings or in more complex systems are commonly attributed to effects such as filler connectivity, interfacial void formation, particle anisotropy, and non-uniform particle size distributions. To partially address these limitations, modified effective-medium models have been proposed, for example, by incorporating shape factors for non-spherical inclusions or

correction terms for non-ideal interfaces; however, these models generally retain the central assumption of non-porous, non-hierarchical filler phases.

In this work, the Maxwell model is employed as a theoretical baseline to relate the intrinsic transport properties of the polymer matrix and the MOF filler to the overall membrane performance, and to assess the extent to which the experimental permeation data deviates from the behavior expected for ideal, dilute composites. Unlike the Maxwell framework's assumptions of non-interacting, spherical, impermeable inclusions, the Zn-MOF-74 decorated ZIF-8 filler in our system exhibits two key deviations: i) enhanced polymer-MOF interfacial interactions that facilitate non-classical transport pathways beyond conventional MMMs, and ii) interconnected MOF violate the isolated, spherical inclusion geometry. Consequently, the Maxwell model provides a conservative reference for conventional fillers, whereas our hierarchical Zn-MOF-74@ZIF-8 system demonstrates superior performance driven by these interfacial and morphological effects characteristic of advanced MMM architectures

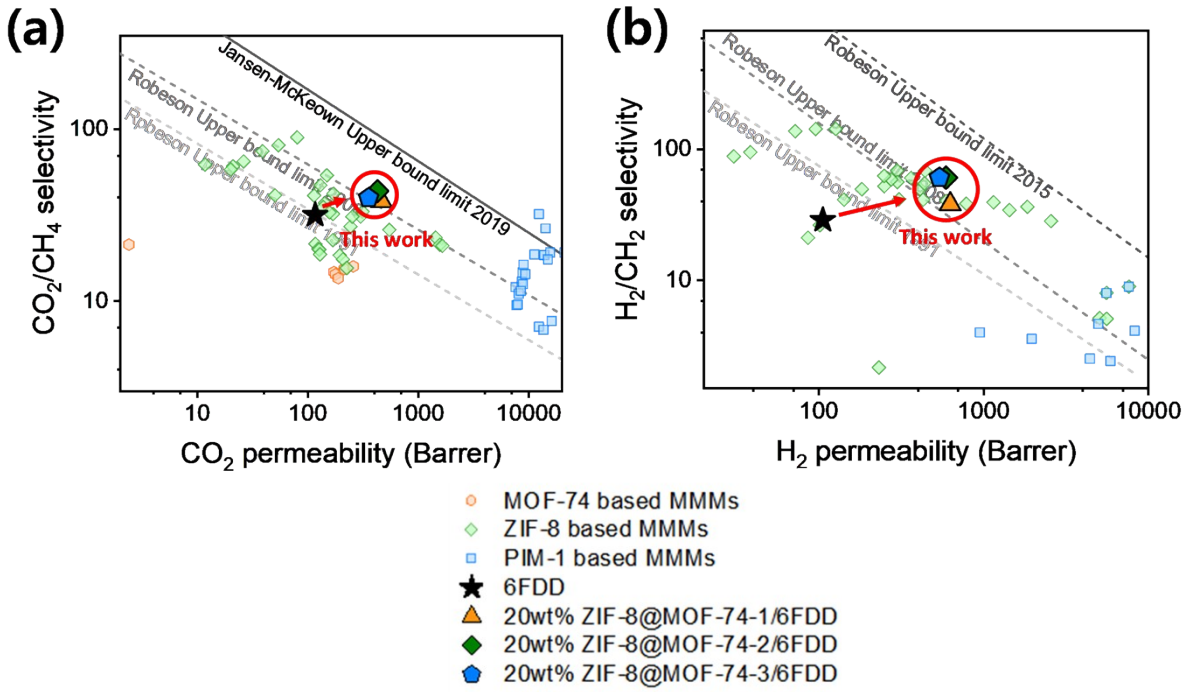

Fig. S24. (a) CO_2/CH_4 and (b) H_2/CH_4 pure gas separation performances at 15 psi and 35 °C with Robeson upper bound permeability limits of 1991, 2008, 2015, and Jansen-McKown upper bound limit 2019 for the pristine 6FDD membrane and series of 20 wt% ZIF8@MOF-74/6FDD MMMs compared to previously reported ZIF-8 and MOF-74-based MMMs. The gray symbols indicate the data obtained from the previously reported literature. [21,24-38]

Table S1. Actual MOF weight loadings in MMMs determined by back-calculation based on

Sample	Actual Weight (%)	Sample	Actual Weight (%)
6FDD	0	**6FDD**	0
10 wt% ZIF-8/6FDD	13 ± 2.4	**20 wt% ZIF-8/6FDD**	24 ± 0.7
10 wt% ZIF-8@MOF-74-1/6FDD	14 ± 2.4	**20 wt% ZIF-8@MOF-74-1/6FDD**	23 ± 2.3
10 wt% ZIF-8@MOF-74-2/6FDD	13 ± 3.1	**20 wt% ZIF-8@MOF-74-2/6FDD**	22 ± 1.7
10 wt% ZIF-8@MOF-74-3/6FDD	13 ± 3.5	**20 wt% ZIF-8@MOF-74-3/6FDD**	22 ± 2.6

TGA results.

Table S2. Mechanical properties of the pure 6FDD polyimide membrane and the 10 wt% ZIF-8/6FDD and ZIF-8@MOF-74-3/6FDD MMMs.

Sample	Yield Strength (MPa)	Young's Modulus (MPa)	Elongational at Break (%)	Tensile Strength (MPa)
6FDD	42.1	12.6	7.5	53.6
10 wt% ZIF-8/6FDD	19.2	11.5	1.8	20.6
10 wt% ZIF-8@MOF-74-3/6FDD	29.1	12.6	2.8	30.7

Table S3. N_2, CH_4, and CO_2 diffusivities, and CO_2/N_2 and CO_2/CH_4 diffusivity-selectivity values for the 6FDD polyimide membrane, 20 wt% ZIF-8/6FDD and series of 20wt% ZIF-8@MOF-74/6FDD MMMs with 10 or 20 wt% MOF loading at 15 psi and 35 °C.

Sample	$D(N_2)$	$D(CH_4)$	$D(CO_2)$	$D(CO_2)$ / $D(N_2)$	$D(CO_2)$ / $D(CH_4)$
6FDD	5.3 ± 0.5	1.2 ± 0.2	32.5 ± 2.5	6.2 ± 01	27.1 ± 0.2
10 wt% ZIF-8/ 6FDD MMM	10.5 ± 0.5	24. ± 0.2	78.5 ± 4.5	7.5 ± 0.1	33.4 ± 0.2
10 wt% ZIF-8@MOF-74-1/6FDD MMM	19.5 ± 1.5	3.9 ± 0.3	142 ± 10	7.3 ± 0.1	36.8 ± 0.1
10 wt% ZIF-8@MOF-74-2/6FDD MMM	18.5 ± 0.8	3.7 ± 0.2	138 ± 5	7.5 ± 0.1	37.8 ± 0.2
10 wt% ZIF-8@MOF-74-3/6FDD MMM	14.5 ± 0.5	2.9 ± 0.1	112 ± 4	7.72 ± 0.01	38.0 ± 0.1
20 wt% ZIF-8/ 6FDD MMM	17.5 ± 0.5	2.9 ± 0.1	105 ± 6	6.0 ± 0.1	36.0 ± 0.7
20 wt% ZIF-8@MOF-74-1/6FDD MMM	99.5 ± 6.5	22.5 ± 1.5	340 ± 22	3.42 ± 0.01	15.1 ± 0.1
20 wt% ZIF-8@MOF-74-2/6FDD MMM	80.5 ± 6.5	7.6 ± 0.6	289 ± 24	3.59 ± 0.01	38.0 ± 0.1
20 wt% ZIF-8@MOF-74-3/6FDD MMM	25.5 ± 1.5	4.5 ± 0.2	212 ± 11	8.30 ± 0.08	47.0 ± 0.2

The diffusivity (D) values are reported as 10^{-8} cm^2/s.

Table S4. N_2, CH_4, and CO_2 solubilities, and CO_2/N_2 and CO_2/CH_4 solubility-selectivity values for the 6FDD polyimide membrane, 20 wt% ZIF-8/6FDD and series of 20 wt% ZIF-8@MOF-74/6FDD MMMs with 10 or 20 wt% MOF loading at 15 psi and 35 °C.

Sample	$S(N_2)$	$S(CH_4)$	$S(CO_2)$	$S(CO_2)$ / $S(N_2)$	$S(CO_2)$ / $S(CH_4)$
6FDD	0.65 ± 0.01	2.3 ± 0.1	2.7 ± 0.1	4.19 ± 0.03	1.16 ± 0.01
10 wt% ZIF-8/ 6FDD MMM	0.400 ± 0.003	1.28 ± 0.01	1.21 ± 0.01	3.03 ± 0.01	0.947 ± 0.003
10 wt% ZIF-8@MOF-74-1/6FDD MMM	0.454 ± 0.004	1.65 ± 0.01	1.66 ± 0.02	3.66 ± 0.01	1.00 ± 0.01
10 wt% ZIF-8@MOF-74-2/6FDD MMM	0.477 ± 0.05	1.61 ± 0.01	1.55 ± 0.01	3.25 ± 0.01	0.966 ± 0.002
10 wt% ZIF-8@MOF-74-3/6FDD MMM	0.521 ± 0.03	1.71 ± 0.01	1.59 ± 0.1	3.04 ± 0.2	0.929 ± 0.066
20wt% ZIF-8/ 6FDD MMM	0.522 ± 0.01	2.09 ± 0.02	1.69 ± 0.01	3.24 ± 0.01	0.808 ± 0.004
20 wt% ZIF-8@MOF-74-1/6FDD MMM	0.146 ± 0.02	0.41 ± 0.01	1.03 ± 0.02	7.11 ± 0.01	2.56 ± 0.01
20 wt% ZIF-8@MOF-74-2/6FDD MMM	0.162 ± 0.04	0.97 ± 0.03	1.12 ± 0.03	6.93 ± 0.02	1.149 ± 0.002
20 wt% ZIF-8@MOF-74-3/6FDD MMM	0.448 ± 0.04	1.50 ± 0.01	1.27 ± 001	2.84 ± 0.01	0.849 ± 0.002

The solubility (S) values are reported as 10^{-2} cm^3(STP)/cm^3·cmHg.

Table S5. CO_2/N_2 and CO_2/CH_4 sorption(***S***) selectivity of ZIF-8 and ZIF-8@MOF-74-3 nanoparticles at 308.15K.

Sample	***S*(CO_2) / ***S*(N_2)**	***S*(CO_2) / ***S*(CH_4)**
ZIF-8	6.4	2.6
ZIF-8@MOF-74-3	9.7	3.0

Table S6. Pure- and mixed-gas transport properties of 6FDD and 20 wt% ZIF-8@MOF-74-1/6FDD at 25 °C.

Sample	Pure-gas (2 atm)			Mixed-gas (4 atm, equimolar CO_2/CH_4)		
	CO_2 (Barrer)	CH_4 (Barrer)	CO_2/CH_4	CO_2 (Barrer)	CH_4 (Barrer)	CO_2/CH_4
6FDD	140	4.4	32	160	5.5	29
20 wt% ZIF-8@MOF-74-1/6FDD MMM	540	15.2	36	520	13.1	40

Table S7. Gas separation performance of MOF-74-, ZIF-8-, and PIM-1-based MMMs reported in the literature.

	Sample	Test conditions	Permeability (Barrer)			Selectivity		References
			$P(H_2)$	$P(CO_2)$	$P(CH_4)$	$P(CO_2)$ / $P(CH_4)$	$P(H_2)$ / $P(CH_4)$	
MOF-74 based MMMs	2wt% Pebax/Ni(Zn)-MOF-74-2	35 °C Mixed gas (50:50)		216.0	14.10	15.32		[24]
	2wt% Pebax/Ni(Zn)-MOF-74-21			260.3	16.43	15.84		
	2wt% Pebax/Ni(Zn)-MOF-74-11			174.2	11.86	14.69		
	2wt% Pebax/Ni(Zn)-MOF-74-12			179.5	12.61	14.23		
	2wt% Pebax/Zn-MOF-74			190.3	14.10	13.50		
	5wt% Mg-MOF-74/PVAc	35 °C 11 bar Single gas		0.86	0.07	12.00		[25]
	15wt% Mg-MOF-74/PVAc			1.72	0.11	15.60		
	20wt% Mg-MOF-74/PVAc			2.42	0.11	21.20		
ZIF-8 based MMMs	2wt% ZIF-8/Pebax	Single gas		117.9	5.50	21.40		[26]
	3wt% ZIF-8/Pebax			125.7	6.30	20.00		
	4wt% ZIF-8/Pebax			128.4	6.50	19.80		
	5wt% ZIF-8/Pebax			130.0	7.0	18.60		
	10wt% ZIF-8/ODPA-TMPDA	25 °C 1 bar Single gas		144.0	3.89	37.00		[27]
	20wt% ZIF-8/ODPA-TMPDA			246.0	9.11	27.00		
	30wt% ZIF-8/ODPA-TMPDA			316.0	9.58	33.00		
	10wt% ZIF-8/ODPA-TMPDA			131.0	2.79	47.00		
	20wt% ZIF-8/ODPA-TMPDA			172.0	4.10	42.00		
	30wt% ZIF-8/ODPA-TMPDA			115.0	2.80	41.00		
	16.7wt% ZIF-8@CA	25 °C 0.3 Mpa Single gas		170.2	7.6	22.50		[28]
	16.7wt% PEI-grafted ZIF-8@CA			150.3	2.80	53.7		
	30wt% ZIF-8@PDA/TB	35 °C 4.5 bar Single gas	478.6	196.2	10.66	18.40	44.9	[29]
	40wt% ZIF-8@PDA/TB		542.25	209.6	12.05	17.40	45.0	
	50wt% ZIF-8@PDA/TB		674.45	277.3	17.89	15.50	37.7	
	10wt% ZIF-8-NH_2/6FBDA	6 bar Single gas	30.6	21.2	0.35	60.60	87.4	[30]
	20wt% ZIF-8-NH_2/6FBDA		28.5	26.4	0.41	64.60	93.9	
	30wt% ZIF-8-NH_2/6FBDA		72.2	39.3	0.53	74.20	136.2	
	40wt% ZIF-8-NH_2/6FBDA		96.1	54.7	0.68	80.40	141.3	
	50wt% ZIF-8-NH2/6FBDA		127.5	80.8	0.9	89.40	141.7	
	10wt% ZIF-8/6FDD	35 °C	182	139.3	4.0	35.10	45.8	[31]

	20wt% ZIF-8/6FDD	15 psi	254	170.7	5.3	32.40	48.2	
	30wt% ZIF-8/6FDD	Single gas	424	303.1	9.8	30.90	43.2	
	10wt% ZIF-8-NH_2/6FDD		185	158.7	4.9	32.70	38.2	
	20wt% ZIF-8-NH_2/6FDD		336	255.5	8.3	30.90	40.7	
	30wt% ZIF-8-NH_2/6FDD		762	552.4	21.3	25.90	35.7	
	3wt% ZIF-8/6FDA-durene	6 bar Single gas		1449.7	62.1	23.34		[32]
	5wt% ZIF-8/6FDA-durene			1582.8	74.7	21.19		
	7wt% ZIF-8/6FDA-durene			1671.6	80.1	20.87		
	10wt% ZIF-8/6FDA-BI	35 °C		11.8	0.19	62.11		[33]
	20wt% ZIF-8/6FDA-BI	4 bar		20.3	0.35	58.00		
	30wt% ZIF-8/6FDA-BI	Single gas		50.9	1.24	41.05		
	9wt% MIL-101/PIM-1	25 °C	955	2830	241	11.74	3.96	[34]
	17wt% MIL-101/PIM-1	1 bar	1970	5940	556	10.68	3.54	
	23wt% MIL-101/PIM-1	Single gas	2880	8310	706	11.77	4.08	
	10wt% MOF-808/PIM-1	35 °C 3 bar Single gas		11370	612	18.6		[21]
	10wt% MOF-808@Lys			14354	543	26.4		
	10wt% MOF-808@Arg			14056	762	18.5		
	10wt% MOF-808@Cst			13877	749	18.5		
	2wt% MUF-15@PIM-1	20 °C	4450	12470	1770	7.06	2.5	[35]
	5wt% MUF-15@PIM-1	1 bar	5000	16310	2140	7.62	4.6	
	10wt% MUF-15@PIM-1	Single gas	5920	16740	2470	6.77	2.4	
PIM-1 based MMMs	20wt% UiO-66-NH_2/PIM-1	25 °C		7660	638	12.0		[36]
	PIM-co-UiO-66-12h	2 bar		15815	828	19.1		
	PIM-co-UiO-66-72h	Single gas		12498	392	31.9		
	2.5% UiO-66/PIM-1	35 °C 3 bar		7842	839	9.4		[37]
	5% UiO-66/PIM-1			8225	746	11.0		
	7.5% UiO-66/PIM-1			8753	680	12.9		
	10% UiO-66/PIM-1			8995	723	12.5		
	2.5% MOF-808/PIM-1			8053	846	9.5		
	5% MOF-808/PIM-1			8579	755	11.4		
	7.5% MOF-808/PIM-1			8897	611	14.6		
	10% MOF-808/PIM-1			9090	563	16.2		
	10% MOF-74@PIM-1	25 °C Single gas	5611	9400	707	14.3	7.9	[38]
	15% MOF-74@PIM-1		7670	15064	866	17.4	8.86	
	20% MOF-74@PIM-1		11469	21269	1114	19.1	10.29	

References

[1] S. Lawson, A. Siemers, J. Kostlenick, Q. Al-Naddaf, K. Newport, A.A. Rownaghi, F. Rezaei, Mixing Mg-MOF-74 with Zn-MOF-74: A Facile Pathway of Controlling the Pharmacokinetic Release Rate of Curcumin, ACS Appl. Bio Mater. 4 (2021) 6874-6880.

[2] O. Karagiaridi, M.B. Lalonde, W. Bury, A.A. Sarjeant, O.K. Farha, J.T. Hupp, Opening ZIF-8: A Catalytically Active Zeolitic Imidazolate Framework of Sodalite Topology with Unsubstituted Linkers, J. Am. Chem. Soc. 134 (2012) 18790-18796.

[3] G. Liu, Y. Qin, L. Jing, G. Wei, H. Li, Two novel MOF-74 analogs exhibiting unique luminescent selectivity, Chem. Comm. 49 (2013) 1699-1701.

[4] X. Yu, J. Li, M. Du, X. Song, H. Huang, L. Nie, Adaptive lattice-matched MOF and COF core-shell heterostructure for carbon dioxide photoreduction, Cell Rep. Phys. Sci. 4 (2023).

[5] C. Guo, C. Liang, X. Qin, Y. Gu, P. Gao, M. Shao, W.T. Wong, Zeolitic Imidazolate Framework Cores Decorated with Pd Nanoparticles and Coated Further with Metal-Organic Framework Shells (ZIF-8@Pd@MOF-74) as Nanocatalysts for Chemoselective Hydrogenation Reactions, ACS Appl. Nano Mater. 3 (2020) 7242-7251.

[6] F. Frati, M.O.J.Y. Hunault, F.M.F. De Groot, Oxygen K-edge X-ray Absorption Spectra, Chem. Rev. 120 (2020) 4056-4110.

[7] Y. Jiang, L. Chen, C. Xiao, N. Zhou, T. Qing, L. Qian, Friction and Wear Behaviors of Steel Ball Against Polyimide-PTFE Composite Under Rolling-Sliding Motion, Tribol. Lett. 69 (2021) 100.

[8] X. Li, J. Zhang, Y. Han, M. Zhu, S. Shang, W. Li, MOF-derived various morphologies of N-doped carbon composites for acetylene hydrochlorination, J. Mater. Sci. 53 (2018) 4913-4926.

[9] Y. Chen, X. Song, N. Zhang, X. Zhang, G. Su, M. Huang, H. Jiang, Polyethyleneimine-Mediated Polyamide Composite Membrane with High Perm-Selectivity for Forward Osmosis, Macromol. Mater. Eng. 306 (2021).

[10] K. Archana Yadav, G. Mishra, S. Kundu, S. Ghosh, R. Haldar, Spatial functionality gradient in a ZIF-8 thin film membrane, Chem. Sci. 16 (2025) 18161-18166.

[11] Q. Liu, X. Gao, Z. Liu, L. Gai, Y. Yue, H. Ma, Sensitive and Selective Electrochemical Detection of Lead(II) Based on Waste-Biomass-Derived Carbon Quantum Dots@Zeolitic Imidazolate Framework-8, Materials 16 (2023).

[12] J. Peng, Z. Zhang, C. Hu, Z. Wang, Y. Kang, W. Chen, T. Ao, Hierarchically porous ZIF-8 for tetracycline hydrochloride elimination, J. Solgel Sci. Technol. 99 (2021) 339-353.

[13] S. Gadipelli, Z. Guo, Postsynthesis annealing of MOF-5 remarkably enhances the framework structural stability and CO2 uptake, Chem. Mat. 26 (2014) 6333-6338.

[14] P. Karthik, R. Vinoth, P. Zhang, W. Choi, E. Balaraman, B. Neppolian, π-π Interaction between Metal-Organic Framework and Reduced Graphene Oxide for Visible-Light Photocatalytic H2 Production, ACS Appl. Energy Mater. 1 (2018) 1913-1923.

[15] L.K. Njaramba, Y. Yoon, C.M. Park, Fabrication of porous beta-cyclodextrin functionalized PVDF/Fe-MOF mixed matrix membrane for enhanced ciprofloxacin removal, NPJ Clean Water 7 (2024).

[16] M.W. Gaultois, A.P. Grosvenor, Coordination-induced shifts of absorption and binding energies in the SrFe1- xZnxO3-δ system, J. Phy. Chem. C 114 (2010) 19822-19829.

[17] J. Dechnik, C.J. Sumby, C. Janiak, Enhancing Mixed-Matrix Membrane Performance with Metal-Organic Framework Additives, Cryst. Growth Des. 17 (2017) 4467-4488.

[18] H. Rabiee, S. Meshkat Alsadat, M. Soltanieh, S.A. Mousavi, A. Ghadimi, Gas permeation and sorption properties of poly(amide-12-b-ethyleneoxide)(Pebax1074)/SAPO-34 mixed matrix membrane for CO2/CH4 and CO2/N2 separation, J. Ind. Eng. Chem. 27 (2015) 223-239.

[19] H.M. Khalid, A. Mujahid, A. Ali, A.L. Khan, M. Saleem, R.M. Santos, Development of Mixed Matrix Membranes by Using NH2-Functionalized UiO-66 and [APTMS][AC] Ionic Liquid for the Separation of CO2, Int. J. Energy Res. 2024 (2024).

[20] M.Z. Ahmad, T.A. Peters, N.M. Konnertz, T. Visser, C. Téllez, J. Coronas, V. Fila, W.M. de Vos, N.E. Benes, High-pressure CO2/CH4 separation of Zr-MOFs based mixed matrix membranes, Sep. Purif. Technol. 230 (2020).

[21] D. Refaat, M. Yahia, H.D. Martínez-Hernández, M. Jimenez-Ruiz, V. Galván, V. Petrenko, R. Fernández de Luis, J. Coronas, Mixed matrix membranes of PIM-1 incorporating MOF-808 functionalized with amino acids for enhanced CO2/CH4separation, J. Mater. Chem. A Mater. 13 (2025) 39254-39270.

[22] Y. Weng, W. Ji, C. Ye, H. Dong, Z. Gao, J. Li, C. Luo, X. Ma, Simultaneously enhanced CO2 permeability and CO2/N2 selectivity at sub-ambient temperature from two novel functionalized intrinsic microporous polymers, J. Membr. Sci. 644 (2022).

[23] J.C. Tan, T.D. Bennett, A.K. Cheetham, Chemical structure, network topology, and porosity effects on the mechanical properties of Zeolitic Imidazolate Frameworks, Proc. Natl. Acad. Sci. U. S. A. 107 (2010) 9938-9943.

[24] S. Majumdar, B. Tokay, V. Martin-Gil, J. Campbell, R. Castro-Muñoz, M.Z. Ahmad, V. Fila, Mg-MOF-74/Polyvinyl acetate (PVAc) mixed matrix membranes for CO2 separation, Sep. Purif. Technol. 238 (2020).

[25] W. Zhu, L. Wang, W. Liang, R. Guo, Z. Li, Bimetallic MOF-74-based mixed matrix membrane for efficient CO2 separation, Micrpor. Mesopor. Mat. 379 (2024).

[26] S. Meshkat, S. Kaliaguine, D. Rodrigue, Comparison between ZIF-67 and ZIF-8 in Pebax® MH-1657 mixed matrix membranes for CO2 separation, Sep. Purif. Technol. 235 (2020).

[27] S.A.S.C. Samarasinghe, C.Y. Chuah, Y. Yang, T.H. Bae, Tailoring CO2/CH4 separation properties of mixed-matrix membranes via combined use of two- and three-dimensional metal-organic frameworks, J. Membr. Sci. 557 (2018) 30-37.

[28] Z. Hu, H. Zhang, X.F. Zhang, M. Jia, J. Yao, Polyethylenimine grafted ZIF-8@cellulose acetate membrane for enhanced gas separation, J. Membr. Sci. 662 (2022).

[29] X. Wang, L. Wu, N. Li, Y. Fan, Sealing Tröger base/ZIF-8 mixed matrix membranes defects for improved gas separation performance, J. Membr. Sci. 636 (2021) 119582.

[30] J.H. Jo, C.O. Lee, G.Y. Ryu, H. Jae, D. Roh, W.S. Chi, Hierarchical Amine-Functionalized ZIF-8 Mixed-Matrix Membranes with an Engineered Interface and Transport Pathway for Efficient Gas Separation, ACS Appl. Polym. Mater. 4 (2022) 6426.

[31] V. Nafisi, M.B. Hägg, Gas Separation Properties of ZIF-8/6FDA-Durene Diamine Mixed Matrix Membrane, Sep. Purif. Technol. 128 (2014) 31.

[32] Y. Fan, H. Yu, S. Xu, Q. Shen, H. Ye, N. Li, Zn(II)-modified imidazole containing polyimide/ZIF-8 mixed matrix membranes for gas separations, J. Membr. Sci. 597 (2020).

[33] N. Tien-Binh, H. Vinh-Thang, X.Y. Chen, D. Rodrigue, S. Kaliaguine, Crosslinked MOF-polymer to enhance gas separation of mixed matrix membranes, J. Membr. Sci. 520 (2016) 941-950.

[34] M. Khdhayyer, A.F. Bushell, P.M. Budd, M.P. Attfield, D. Jiang, A.D. Burrows, E. Esposito, P. Bernardo, M. Monteleone, A. Fuoco, G. Clarizia, F. Bazzarelli, A. Gordano, J.C. Jansen, Mixed matrix membranes based on MIL-101 metal-organic frameworks in polymer of intrinsic microporosity PIM-1, Sep. Purif. Technol. 212 (2019) 545-554.

[35] H. Yin, A. Alkaş, Y. Zhang, Y. Zhang, S.G. Telfer, Mixed matrix membranes (MMMs) using an emerging metal-organic framework (MUF-15) for CO2 separation, J. Membr. Sci. 609 (2020).

[36] N. Tien-Binh, D. Rodrigue, S. Kaliaguine, In-situ cross interface linking of PIM-1 polymer and UiO-66-NH2 for outstanding gas separation and physical aging control, J. Memb. Sci. 548 (2018) 429-438.

[37] M. Yahia, L.A. Lozano, J.M. Zamaro, C. Téllez, J. Coronas, Microwave-assisted synthesis of metal–organic frameworks UiO-66 and MOF-808 for enhanced CO2/CH4 separation in PIM-1 mixed matrix membranes, Sep. Purif. Technol. 330 (2024).

[38] Q. Zhao, Y. Sun, J. Zhang, F. Fan, T. Li, G. He, C. Ma, Mixed matrix membranes incorporating amino-functionalized ZIF-8-NH2 in a carboxylic polyimide for molecularly selective gas separation, J. Membr. Sci. 693 (2024).